PHILOSOPHICAL TRANSACTIONS OF THE ROYAL SOCIETY A MATHEMATICAL, PHYSICAL & ENGINEERING SCIENCES

Linearly Stratified, Rotating Flow over Long Ridges in a Channel

D. L. Boyer and F. M. Biolley

Phil. Trans. R. Soc. Lond. A 1986 **318**, 411-438
doi: 10.1098/rsta.1986.0079

Phil. Trans. R. Soc. Lond. A **318**, 411–438 (1986) [411]
Printed in Great Britain

LINEARLY STRATIFIED, ROTATING FLOW OVER LONG RIDGES IN A CHANNEL

BY D. L. BOYER AND F. M. BIOLLEY
Department of Mechanical Engineering, University of Wyoming, Laramie, Wyoming 82071, *U.S.A.*

(*Communicated by P. H. Roberts, F.R.S. – Received* 10 *April* 1985)

[Plates 1–8]

CONTENTS

The flow of a rotating, linearly stratified fluid over a long symmetric ridge in a channel is investigated experimentally. The laboratory apparatus consists of a long channel of rectangular cross section. The upper bounding surface is a transparent, horizontal plane; the lower boundary is a horizontal flexible belt. The belt serves as a false bottom of the channel and is translated parallel to its long axis. Topographic features are mounted on the belt and are towed through a salt-stratified fluid which is otherwise at rest relative to a rotating observer; the channel rests on a rotating table whose rotation axis is vertical.

The most important dimensionless parameters governing the motion are the Rossby and Ekman numbers, a stratification parameter defined as the ratio of the Brunt–Väisälä frequency to the Coriolis parameter, and the geometrical parameters defining the aspect ratio of the ridge, the ridge height to channel depth ratio and the ridge to channel width ratios.

An analysis is presented that demonstrates the conditions under which centrifugal

effects can be neglected in such laboratory experiments. The analysis also shows the conditions under which the laboratory flows should be a good approximation to the quasigeostrophic potential vorticity equations and attendant boundary conditions for the oceans and atmosphere. This analysis is made for a general three-dimensional topographic feature; i.e. it is not restricted to a long ridge. The laboratory system seems to be an excellent vehicle for modelling oceanic flows but does not properly reproduce a non-Boussinesq term in the atmospheric equation.

An analysis for an infinitely long ridge is presented. The predictions so obtained are in good qualitative agreement with the experiments. The quantitative agreement, for the range of parameters considered however, is shown to be poor and this is attributed to neglecting the effects of the lateral bounding surfaces.

The experiments demonstrate that for fixed rotation, stratification and free stream speed, the streakline deflection caused by the topography decays with height. For such experiments the flow in the lower levels for positive upward rotation deflects to the left before reaching the ridge, then continues to deflect to the left on the upwind side of the ridge before beginning a rightward drift slightly upstream of the mountain crest. This rightward drift continues on the downwind side of the ridge and well downstream of the ridge itself before reaching a maximum shift, from which a leftward drift again begins. Increased rotation, other parameters being held fixed, provides stronger horizontal streakline deflections. Stronger stratification, other parameters being fixed, leads to stronger downslope winds and possibly flow separation in the lee. Various characteristics of the flow field, such as the distance upstream to which substantial streakline curvature is observed, are measured as functions of the various system parameters; comparisons with the infinite ridge theory are also made.

The downstream motion is accompanied by lee waves for the major portion of the parameter space examined. The amplitude of these waves is shown to decrease with increased rotation, other parameters being held fixed. Some non-rotating experiments are conducted and these are shown to be in good agreement with the model of Long (1955) and the measured wavelengths are found to be in good agreement with linear theory and laboratory measurements made by other investigators. Measurements supporting the theory of Queney (1947) are presented which show that the horizontal wavelengths of the lee waves decrease for increased rotation, other parameters being fixed. A flow régime map based on the observed structure of the vertical wave motion is developed and it is shown that for the range of parameters considered, rotation plays only a minor role, if any.

1. Introduction

The effect of topography on the motion of rotating and/or stratified fluids has received a great deal of attention for many years. This interest has generally been motivated by the importance of terrain features in influencing atmospheric and oceanographic current systems. For the most part, research has been addressed to the effects of either rotation or stratification, each taken separately. Studies combining these effects are few in number and this is especially so for laboratory experiments, the principal subject of the present paper. An excellent starting point for the study of terrain effects, especially with regard to atmospheric applications, is the review monograph of Smith (1979).

A thorough review of the laboratory studies of rotating and/or stratified flow past topography was recently made by Baines & Davies (1980). The most noteworthy investigations in the context of the present study, were those experiments of Davies (1972), in which the effect of stratification on Taylor column formation was investigated by towing spheres through a rotating and stratified fluid. Mason (1975) measured the forces on spheres translating horizontally through a rotating stratified fluid. Experiments have also been conducted by

PHILOSOPHICAL TRANSACTIONS OF THE ROYAL SOCIETY A MATHEMATICAL, PHYSICAL & ENGINEERING SCIENCES

inserting topographic features into the non-uniform baroclinic flow of a differentially heated annulus (see, for example, Hide (1966), Fultz & Spence (1967), Yeh & Chang (1974) and Leach (1981)).

The present study is addressed to investigating the flow of a linearly stratified fluid over a long ridge of constant cross section. The ridge extends across the entire width of the channel used for the experiments. Although the channel is substantially wider than the streamwise extent of the ridge, it must be stated at the outset that the existence of the channel sidewalls has an important effect on the overall flow. We recall here the earlier study by one of us (Boyer 1971), in which the sidewalls were neglected for the flow of a homogeneous fluid over a ridge. Although the theoretical model for an 'infinite ridge' gave good qualitative agreement with laboratory experiments, it was later shown by Huppert & Stern (1974) that better quantitative agreement with theory could be obtained with the inclusion of sidewalls. In fact Huppert & Stern concluded that the sidewalls were important no matter what the wall separation distance in relation to the ridge width.

As will be noted below, the situation with the rotating stratified flow is similar in that a theoretical solution can readily be obtained for the infinite ridge case but that predictions so made are only in qualitative agreement with experiment, with certain quantitative comparisons not being good.

The present study is motivated by a number of meteorological situations including the flow over such large-scale ridge-like features as the Rocky Mountains and mesoscale features as the Sierra Nevada Mountains. The latter terrain feature, for example, gives rise to the so-called barrier wind effect. Marwitz (1983) presents a series of aircraft measurements that demonstrate that under both stable and neutrally stable atmospheric conditions, the westerly winds impinging on the Sierra Nevadas (essentially a north–south ridge of an approximately constant cross section) veer sharply to the north at the lower levels in a 'jet-like' fashion. Schwerdtfeger (1974, 1975) noted similar phenomena for the Brooks Range in Alaska and the Antarctic Peninsula in Antarctica, respectively. Parish (1982) developed a numerical model that nicely predicts the barrier winds for the Sierra Nevadas (see also Waight 1984). Pierrehumbert & Wyman (1985) discuss, in non-dimensional terms, the general criteria for the formation of strong barrier winds.

These atmospheric observations can be contrasted with the rotating flow of a homogeneous fluid normal to an infinite ridge in which a westerly flow would veer to the south in the Northern Hemisphere (see Boyer 1971). In the homogeneous case the flow on passing over the ridge encounters a 'Venturi effect', thus increasing its speed owing to continuity considerations. The resulting increased Coriolis force tends to drive the flow to the 'south'. Similar flow deflections can be predicted from arguments of conservation of potential vorticity.

The barrier effect as observed in the atmosphere and as predicted in Parish's (1982) model is thus a phenomenon requiring both rotation and stratification for its explanation. Quite simply, stratification tends to block the westerly flow at the lower levels thus decreasing the Coriolis force in comparison to the north–south pressure gradient and hence causing the flow to veer toward the north. This blocking can occur upstream of the ridge with the result that flow curvature toward the north can be observed in the upstream region (see below). In spite of the relative simplicity of the present laboratory model, it is gratifying that the gross characteristics of the barrier effect can be demonstrated.

A substantial literature on the flow of a rotating and stratified fluid past a long ridge is

PHILOSOPHICAL TRANSACTIONS OF THE ROYAL SOCIETY A MATHEMATICAL, PHYSICAL & ENGINEERING SCIENCES

beginning to accumulate. The classic work on the subject is the linear analysis of Queney (1947), in which the fluid medium is not bounded from above. Many subsequent theoretical analyses are based on this model. Robinson (1960) carried out an inviscid analysis at small Rossby number of the flow over a finite amplitude wavy wall with the fluid being confined from above by a rigid horizontal surface. Jacobs (1964) extended this with an analysis of the flow over a long isolated ridge, again employing the rigid lid and inviscid assumptions. Jacobs demonstrated, for example, that the resulting lee waves become of negligibly small amplitude as the Rossby number is made sufficiently small; this phenomenon is demonstrated experimentally below. Jacobs also showed that westerly winds impinging on a north–south ridge will veer to the north in the lower levels of the fluid; this phenomenon is also observed in our experiments and as noted above is a common feature in atmospheric motions.

Merkine (1975), again using the rigid lid and inviscid conditions, considered the vertically sheared as well as the uniform flow past a large mountain in a rotating stratified atmosphere. Merkine concentrated on a scale analysis of the problem and paid particular attention to the 'far field'. His most important conclusions in the context of the present study were that (i) the flow is permanently deflected to the right (facing downstream with vertically upward rotation) on the lee side of the mountain and (ii) the disturbance created by the mountain extends upstream to several radii of deformation, $L_R = NH/f$, where N is the Brunt–Väisälä frequency, H is the fluid depth and f the Coriolis parameter; this latter result is obtained for regions of parameter space in which the rigid lid is important (for the infinite height case see Pierrehumbert (1985)). Merkine also concludes that for an increase in stratification and for fixed topography and rotation, the mountain will have a greater upstream influence. Our infinite ridge model is in consonance with this result, but for the range of parameters considered in the present experiments and within the accuracy of the observations this theoretical prediction is not noted.

Mason & Sykes (1978) made a numerical analysis of the flow over a long ridge and included the effect of Ekman suction along the lower bounding surface including the ridge. Their results also demonstrated the barrier wind effect of turning a westerly flow toward the north on approaching the ridge.

Pierrehumbert (1984, 1985) considers the flow past a mesoscale ridge. In his 1984 study, using the Queney (1947) model with the fluid unbounded in the vertical, he discusses how the flow depends on the Rossby Number, $Ro_p = 2U/fD$, and Froude number, $Fr_p = Nh/U$; note that the subscript p is used to identify the parameters defined by Pierrehumbert, to distinguish them from other similar parameters defined below. Here U is the free stream speed and D and h are the ridge width and height respectively. A principal conclusion is that the maximum height rather than a smoothed orography should be used in modelling atmospheric flows. In Pierrehumbert (1985), using an analysis similar to that of Jacobs (1964) and Merkine (1975), but considering a semi-infinite atmosphere, he shows that the quasigeostrophic approximation reduces the problem to a single parameter one, that parameter being the Burger number $Ro_p Fr_p = 2hN/fD$, based on the mountain slope. As first noted by Robinson (1960), the quasigeostrophic approximation breaks down by the occurrence of infinite velocities in the vicinity of the ridge crest. Pierrehumbert (1985) shows that the critical values of the Burger number $(Ro_p Fr_p)_{crit}$ are 1.00 and 0.89 for bell-shaped and Gaussian mountains respectively. In Pierrehumbert & Wyman (1985) the quasigeostrophic approximation is relaxed and it is found that the flow at the crest is non-singular, although strong downslope winds are developed.

The plan for the remainder of this paper is as follows. In §2 we consider the governing equations for a salt-stratified laboratory model including diffusion and centrifugal effects. The objectives here are to consider carefully the conditions under which the laboratory model is a good approximation to the quasigeostrophic equations and boundary conditions for the atmosphere and ocean as given in Pedlosky's (1979) book. For example, it is clear that some restrictions must be placed on the level of the background rotation if centrifugal effects are to be truly negligible. In §3 we discuss the modelling criteria for the atmosphere and ocean in terms of the laboratory model. Although the limitations of an infinite ridge model are recognized we present such a model in §4, so that some comparisons can be made with experiment. In §5 we briefly describe the experimental apparatus and discuss the various experimental techniques employed. The experimental results are then presented in §6 and finally an atmospheric example and some concluding remarks are given in §7.

2. Governing equations

The physical system under consideration is sketched in figure 1. We imagine that at time $t^* < 0$ a continuously stratified fluid is confined between two horizontal plane surfaces separated by a depth H and two parallel vertical surfaces separated by a width L (i.e. at

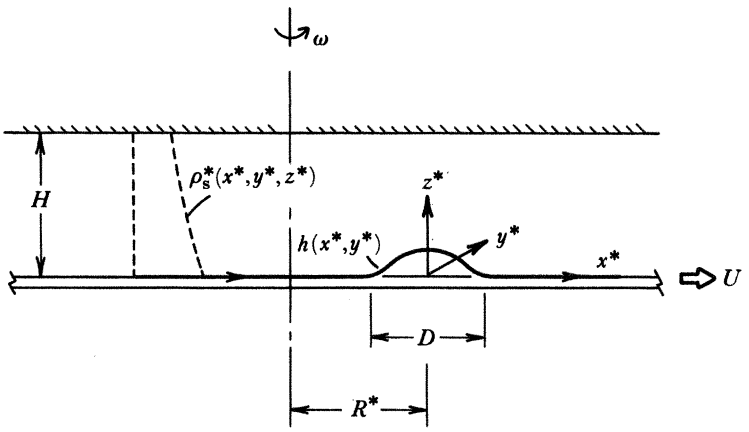

Figure 1. Physical system.

$y^* = \pm\frac{1}{2}L$), and that the fluid is in solid-body rotation, ω, about a vertical axis. At time $t^* = 0$ the lower surface is given an impulsive velocity U in the $+x^*$ direction and this velocity is maintained for $t^* > 0$. A smooth topographic feature of height $h(x^*, y^*)$ is mounted on and translated with the lower surface; note that we consider here a topography of general shape and later will restrict to a long ridge. We denote dimensional independent and dependent variables with asterisks and define (x^*, y^*, z^*) as the rectangular cartesian coordinates fixed to the lower surface. The distance between the axis of rotation and the origin of (x^*, y^*, z^*) is defined as $R^* = Ut^*$. The stratification in the 'rest state' (i.e. $t^* < 0$) is given by $\rho_s^*(x^*, y^*, z^*)$.

In the rest state the density and pressure surfaces must coincide and it is easy to show that

$$\rho_s^*(x^*, y^*, z^*) = \rho_s^*(\zeta^*), \tag{2.1}$$

where

$$\zeta^* = z^* - \omega^2 r^{*2}/2g$$

and where $r^{*2} = (R^* + x^*)^2 + y^{*2}$ and g is the acceleration due to gravity. It is assumed that the background density distribution $\rho_s^*(\zeta^*)$ can be specified experimentally in a wide range of stable stratifications (i.e. ρ_s^* is a decreasing monotonic function of ζ^*). The background pressure distribution $p_s^*(x^*, y^*, z^*) = p_s^*(\zeta^*)$ is then given by

$$\mathrm{d}p_s^*/\mathrm{d}\zeta^* = -\rho_s^* g. \tag{2.2}$$

We now wish to write the dimensionless equations of motion in terms of a coordinate system (x^*, y^*, z^*) which is translating at a constant velocity $U\hat{\imath}$ with respect to the rotating frame. To this end we introduce the following dimensionless quantities:

$$(x, y, z) = \left(\frac{x^*}{D}, \frac{y^*}{D}, \frac{z^*}{H}\right), \quad \zeta = \frac{\zeta^*}{H}, \tag{2.3}$$

$$R = \frac{R^*}{D}, \quad t = \frac{U}{D} t^*, \tag{2.4}$$

and

$$\bar{v}(u, v, w) = \left(\frac{u^*}{U}, \frac{v^*}{U}, \frac{D}{H}\frac{w^*}{U}\right). \tag{2.5}$$

We further define the perturbation density, $\tilde{\rho}^*$, and pressure, $\tilde{p}^*$, fields due to the motion of the lower surface and topography as

$$\rho^* = \rho_s^* + \tilde{\rho}^* \tag{2.6}$$

and

$$p^* = p_s^* + \tilde{p}^* \tag{2.7}$$

respectively, where ρ^* and p^* are the 'total' density and pressure respectively. Anticipating the importance of rotation we introduce the following dimensionless quantities

$$\tilde{\rho} = \tilde{\rho}^* g / 2\omega U \rho_s^*, \quad \tilde{p} = \tilde{p}^* / 2\omega U D \rho_s^* \tag{2.8}$$

respectively. Assuming constant coefficients of viscosity, ν, and diffusion, κ, and substituting (2.1)–(2.8) into the relations for momentum conservation (x, y, z), diffusion and conservation of mass, one obtains

$$(Ro + Fr^2\tilde{\rho})\frac{\mathrm{D}u}{\mathrm{D}t} = -\frac{\partial \tilde{p}}{\partial x} + \left(1 + \frac{Fr^2}{Ro}\tilde{\rho}\right)v + \frac{Fr^2}{4Ro^2}(R + x)\tilde{\rho} + E\left(1 + \frac{Fr^2}{Ro}\tilde{\rho}\right)\frac{H^2}{D^2}\nabla_0^2 u, \tag{2.9}$$

$$(Ro + Fr^2\tilde{\rho})\frac{\mathrm{D}v}{\mathrm{D}t} = -\frac{\partial \tilde{p}}{\partial y} - \left(1 + \frac{Fr^2}{Ro}\tilde{\rho}\right)(1 + u) + \frac{Fr^2}{4Ro^2} y\tilde{\rho} + E\left(1 + \frac{Fr^2}{Ro}\tilde{\rho}\right)\frac{H^2}{D^2}\nabla_0^2 v, \tag{2.10}$$

$$(Ro + Fr^2\tilde{\rho})\frac{\mathrm{D}w}{\mathrm{D}t} = -\frac{D^2}{H^2}\frac{\partial \tilde{p}}{\partial z} - \frac{D}{H}\tilde{\rho} + E\left(1 + \frac{Fr^2}{Ro}\tilde{\rho}\right)\frac{H^2}{D^2}\nabla_0^2 w, \tag{2.11}$$

$$Ro\frac{\mathrm{D}\tilde{\rho}}{\mathrm{D}t} + B^2\frac{H}{D}\left(1 + \frac{Fr^2}{Ro}\tilde{\rho}\right)\left(\frac{Fr^2}{4Ro^2}\frac{D}{H}[(R + x)u + yv] - w\right) = \frac{E}{\sigma}\frac{H^2}{D^2}\frac{1}{\rho_s^*}\nabla_0^2\left(\frac{Ro}{Fr^2}\rho_s^* + \rho_s^*\tilde{\rho}\right), \tag{2.12}$$

and

$$Ro\frac{\mathrm{D}\tilde{\rho}}{\mathrm{D}t} + B^2\frac{H}{D}\left(1 + \frac{Fr^2}{Ro}\tilde{\rho}\right)\left(\frac{Fr^2}{4Ro^2}\frac{D}{H}[(R + x)u + yv] - w\right) + \frac{Ro^2}{Fr^2}\left(1 + \frac{Fr^2}{Ro}\tilde{\rho}\right)(\nabla \cdot \bar{v}) = 0, \tag{2.13}$$

respectively, where

$$\frac{\mathrm{D}}{\mathrm{D}t} = \frac{\partial}{\partial t} + u\frac{\partial}{\partial x} + v\frac{\partial}{\partial y} + w\frac{\partial}{\partial z}$$

and where $$\nabla_0^2 = \frac{\partial^2}{\partial x^2} + \frac{\partial^2}{\partial y^2} + \frac{D^2}{H^2}\frac{\partial^2}{\partial z^2}.$$

The dimensionless parameters are defined as follows:

$$Ro = U/2\omega D, \quad \text{Rossby number},$$

$$Fr^2 = U^2/gD, \quad \text{Froude number},$$

$$E = \nu/2\omega H^2, \quad \text{Ekman number},$$

$$B^2 = -\left(\frac{1}{H}\frac{g}{\rho_s^*}\frac{\mathrm{d}\rho_s^*}{\mathrm{d}\zeta}\right)\Big/4\omega^2 = \frac{N^2}{f^2} \sim O\left\{\left(\frac{g}{H}\frac{\Delta\rho}{\rho_0}\right)\Big/f^2\right\}, \quad \text{stratification parameter},$$

and

$$\sigma = \nu/\kappa, \quad \text{Prandtl number},$$

where $\Delta\rho$ is taken as the difference in the background density between the bottom and top surfaces along the axis of rotation ($\Delta\rho$ is positive) and ρ_0 is the mean density from bottom to top at this location. Note that for stable stratifications $\mathrm{d}\rho_s^*/\mathrm{d}\zeta$ is negative so that B^2 is a positive function of ζ. In addition to these five dynamical parameters, there are four independent dimensionless geometrical parameters including h/H, h/D, D/L and $R = R^*/D$, so that the physical system includes nine independent dimensionless groupings.

Note that the right hand side of (2.12) contains various derivatives of the background stratification ρ_s^*. Although it turns out that these terms are not important in the present experiments, it should be noted that their appearance seems to suggest the importance of additional dimensionless parameters. For the linearly stratified case these can be described in terms of parameters already defined. For general stratifications second derivatives of ρ_s^* appear and indeed an additional dimensionless parameter must be introduced. This matter will not be pursued further.

Numerous other dimensionless parameters can be defined for the present physical system. They are not independent, however, in that they can be expressed as functions of those parameters defined above. Some of these additional parameters are common in the literature and in fact will be used in the discussions below. These include

$$Re = \frac{UD}{\nu} = \frac{Ro}{E}\frac{D^2}{H^2}, \quad \text{Reynolds number},$$

$$F_i = \frac{U}{NH} = \frac{Ro}{B}\frac{D}{H}, \quad \text{internal Froude number},$$

and

$$S = \frac{N^2}{f^2}\frac{H^2}{D^2} = B^2\frac{H^2}{D^2}, \quad \text{Burger number}.$$

The set of equations (2.9)–(2.13), along with the appropriate boundary conditions, are exceedingly complex and one is led to seek approximations. With a view toward reducing the equations to a form similar to the quasigeostrophic potential vorticity equations for the atmosphere and oceans as given by (6.5.21) and (6.8.11), respectively, in Pedlosky's (1979) book and by considering the capabilities of the laboratory apparatus we now give typical laboratory values of the various dimensional (table 1) and dimensionless (table 2) parameters. Note that R^* is taken as the order of the width of the topography. For measurements made

Table 1. Typical dimensional parameters

$U = 0.5$ cm s^{-1}	$\rho_0 = 1.0$ g cm^{-3}	$D = 10.0$ cm
$\omega = 0.25$ rad s^{-1}	$\Delta\rho = 0.01$ g cm^{-3}	$h = 1.0$ cm
$\nu = 0.01$ cm^2 s^{-1}	$g = 981$ cm s^{-2}	$R^* = 10.0$ cm
$\kappa = 1.6 \times 10^{-5}$ cm^2 s^{-1}	$H = 8.1$ cm	$L = 31.2$ cm

Table 2. Typical dimensionless parameters

$Ro = 0.10$	$B^2 = 4.8$	$H/D = 0.81$
$Fr^2 = 2.6 \times 10^{-5}$	$\sigma^{-1} = 1.6 \times 10^{-3}$	$D/L = 0.32$
$E = 3.0 \times 10^{-4}$	$h/H = 0.12$	$R = 1.0$

far from the axis of rotation considerably larger values should be assigned. This matter is, of course, important in assessing the conditions under which centrifugal effects are important.

There are numerous possibilities for making *a priori* assumptions as to the relative size of the various dimensionless parameters. The following assumptions are consistent with the laboratory experiments and reduce the laboratory equations and boundary conditions to relations quite similar to those governing large-scale motions in the atmosphere and oceans (see Pedlosky 1979).

We begin with the fundamental assumption that the Rossby number is small, i.e. $Ro \ll 1$. Although restrictions on other parameters are also required, the small Ro assumption is essential for the dynamics to be quasigeostrophic. We then anticipate expanding the dependent variables in (2.9)–(2.13) in power series in the Rossby number and will require both a zero-order and a first-order approximation to determine the lowest-order motion. For convenience we thus express the relative size of the remaining parameters in terms of Ro. Let us assume the following:

$$E \leqslant O(Ro^2), \quad B \sim O(1),$$

$$Fr^2 \sim O(Ro^{3+\alpha}), \quad \alpha > 0,$$

$$\sigma^{-1} \sim O(Ro^{\beta}), \quad \beta > 0,$$

$$h/H \sim O(Ro^{\delta}), \quad 0 < \delta \leqslant 1,$$

$$H/D \sim O(1), \quad R \sim O(1),$$

and

$$D/L \sim O(Ro^{\gamma}), \quad \gamma > 0.$$

We will show that when $E \sim O(Ro^2)$, Ekman suction is important for determining the lowest-order motion, whereas for smaller E viscous effects may be neglected. By examining the first-order approximations of (2.9) and (2.10), and by requiring the centrifugal terms to be small compared with, say, the Coriolis terms, we conclude that the Froude number must not be too large, i.e. $Fr^2 \sim O(Ro^{3+\alpha})$, where $\alpha > 0$. This requirement of negligible centrifugal effects may also be written as $\omega^3 D^2/gU \ll 1$. The restriction on the smallness of the inverse Prandtl number ensures that the background stratification will not diffuse substantially during the experiment. Only infinitesimal topographies are considered so that for cases in which Ekman suction is important, that effect can be included in a straightforward manner. For isolated topographies we would like a large separation distance between the terrain feature and the lateral walls so that the latter do not influence the flow in the vicinity of the topography.

We now assume that the dependent variables can be expanded in a power series in the Rossby number, i.e.

$$\bar{v} = \bar{v}_0 + Ro\,\bar{v}_1 + \ldots, \tag{2.14}$$

$$\tilde{p} = (p_0 - y) + Ro\,p_1 + \ldots, \tag{2.15}$$

$$\tilde{\rho} = \rho_0 + Ro\,\rho_1 + \ldots. \tag{2.16}$$

Substituting (2.14)–(2.16) into (2.9)–(2.13) yields the zero-order

$$v_0 = \partial p_0/\partial x, \tag{2.17}$$

$$u_0 = -\partial p_0/\partial y, \tag{2.18}$$

$$\rho_0 = -\frac{D}{H}\frac{\partial p_0}{\partial z}, \tag{2.19}$$

$$w_0 = 0, \tag{2.20}$$

and

$$\partial u_0/\partial x + \partial v_0/\partial y = 0, \tag{2.21}$$

and first-order

$$\frac{\partial u_0}{\partial t} + u_0\frac{\partial u_0}{\partial x} + v_0\frac{\partial u_0}{\partial y} = -\frac{\partial p_1}{\partial x} + v_1, \tag{2.22}$$

$$\frac{\partial v_0}{\partial t} + u_0\frac{\partial v_0}{\partial x} + v_0\frac{\partial v_0}{\partial y} = -\frac{\partial p_1}{\partial y} - u_1, \tag{2.23}$$

$$\rho_1 = -\frac{D}{H}\frac{\partial p_1}{\partial z}, \tag{2.24}$$

$$w_1 = \frac{1}{B^2}\frac{D}{H}\left(\frac{\partial \rho_0}{\partial t} + u_0\frac{\partial \rho_0}{\partial x} + v_0\frac{\partial \rho_0}{\partial y}\right), \tag{2.25}$$

and

$$\frac{\partial u_1}{\partial x} + \frac{\partial v_1}{\partial y} + \frac{\partial w_1}{\partial z} = 0 \tag{2.26}$$

relations, respectively.

By subtracting the derivative of (2.23) with respect to x from that of (2.22) with respect to y and using (2.17)–(2.19), (2.25) and (2.26) we arrive at the following relation for p_0 which, by (2.17) and (2.18), is a streamfunction:

$$\left(\frac{\partial}{\partial t} + \frac{\partial p_0}{\partial x}\frac{\partial}{\partial y} - \frac{\partial p_0}{\partial y}\frac{\partial}{\partial x}\right)\left\{\frac{\partial^2 p_0}{\partial x^2} + \frac{\partial^2 p_0}{\partial y^2} + \frac{\partial}{\partial z}\left(\frac{1}{B^2}\frac{D^2}{H^2}\frac{\partial p_0}{\partial z}\right)\right\} = 0. \tag{2.27}$$

Let us now consider the boundary conditions. Far upstream we require

$$x \to +\infty, \quad u_0 = -1 \quad \text{or} \quad \partial p_0/\partial y = 1, \tag{2.28}$$

whereas far downstream

$$x \to -\infty, \quad v_0 = 0 \quad \text{or} \quad \partial p_0/\partial x = 0. \tag{2.29}$$

Along the lateral walls we require

$$y = \pm L/2D, \quad u_0 = -1 \quad \text{or} \quad \partial p_0/\partial y = 1. \tag{2.30}$$

Along the bottom we let $h(x^*, y^*)/H = Ro^{\delta}\,h_0(x, y)$, where $h_0(x, y) \sim O(1)$. Then using (2.17)–(2.19) and (2.25) and recognizing that the lowest-order interior vertical velocity

evaluated along the lower surface must equal the combined effect of the deflection of fluid particles by the topography and Ekman suction, we can write

$$\frac{1}{B^2}\frac{D^2}{H^2}\left(\frac{\partial^2 p_0}{\partial z\,\partial t}-\frac{\partial p_0}{\partial y}\frac{\partial^2 p_0}{\partial x\,\partial z}+\frac{\partial p_0}{\partial x}\frac{\partial^2 p_0}{\partial y\,\partial z}\right)=-Ro^{\delta-1}\left(\frac{\partial p_0}{\partial x}\frac{\partial h_0}{\partial y}-\frac{\partial p_0}{\partial y}\frac{\partial h_0}{\partial x}\right)-\frac{1}{\sqrt{2}}\frac{E^{\frac{1}{2}}}{Ro}\nabla_2^2 p_0 \quad (2.31)$$

along $(x, y, 0)$, where $\nabla_2^2=\partial^2/\partial x^2+\partial^2/\partial y^2$. Now for 'large slope' topographies for which $\delta<1$ and for $E\leqslant O(Ro^2)$, the first term on the right hand side of (2.31) will dominate and we require

$$\frac{\partial p_0}{\partial x}\frac{\partial h_0}{\partial y}-\frac{\partial p_0}{\partial y}\frac{\partial h_0}{\partial x}=0$$

in the vicinity of the topography. This means the flow must go around rather than over the topography. For $\delta=1$ (i.e. a topography with slope of $O(Ro)$) the first term on the right hand side is the same order as that of the left hand side. For flows in which $E\leqslant O(Ro^2)$ the second term on the right hand side (i.e. Ekman suction) is negligible while for $E\sim O(Ro^2)$ it is the same size as the remaining terms.

Similarly, for the upper bounding surface we can write

$$\frac{1}{B^2}\frac{D^2}{H^2}\left(\frac{\partial^2 p_0}{\partial z\,\partial t}-\frac{\partial p_0}{\partial y}\frac{\partial^2 p_0}{\partial x\,\partial z}+\frac{\partial p_0}{\partial x}\frac{\partial^2 p_0}{\partial y\,\partial z}\right)=\frac{1}{\sqrt{2}}\frac{E^{\frac{1}{2}}}{Ro}\nabla_2^2 p_0 \quad (2.32)$$

along $(x, y, 1)$. As above, the relative size of E with respect to Ro again determines the importance of Ekman suction.

3. Relationship of laboratory model to atmosphere and oceans

We note first that (2.27) is almost identical to Pedlosky's (1979) relation (6.8.11), the quasigeostrophic potential vorticity equation for the ocean. Here, of course, we must neglect the β-term since this vorticity source term cannot be modelled for a continuously stratified fluid in the laboratory. We also note that for similarity the Burger number, S, as defined by Pedlosky (1979), must be the same as the Burger number, $B^2(H^2/D^2)$, as defined in the present study.

Again neglecting the β-term, Pedlosky's (1979) relation (6.5.21) for the atmosphere includes one term, a non-Boussinesq contribution, not included in (2.27). Pedlosky's relation includes an expression

$$\frac{1}{\rho_s}\frac{\partial}{\partial z}\left(\frac{\rho_s}{S}\frac{\partial \psi}{\partial z}\right)=\frac{\partial}{\partial z}\left(\frac{1}{S}\frac{\partial \psi}{\partial z}\right)+\frac{1}{\rho_s}\frac{\partial \rho_s}{\partial z}\frac{1}{S}\frac{\partial \psi}{\partial z}, \quad (3.1)$$

where ρ_s is his background stratification and ψ is the streamfunction corresponding to our p_0. Thus again relating our Burger number, $B^2(H^2/D^2)$, with Pedlosky's S, the laboratory model simulates the atmospheric one except that it does not include the second term on the right hand side of (3.1); the second term arises from compressibility effects, which cannot be modelled in the laboratory. Both terms on the right hand side of (3.1) seem of comparable magnitude in the atmosphere so that it is not clear how much the neglect of the last term will affect the simulation. It is expected that the simulation will be qualitatively similar but it would remain to make analytical or numerical calculations by excluding and then including the non-Boussinesq term and comparing the results.

On the lower boundary of the ocean and atmosphere Pedlosky's relation (6.6.10) boundary condition applies. Neglecting heat sources or sinks this relation is identical to our (2.31) with

and
$$\frac{E^{\frac{1}{2}}}{\sqrt{2}\,Ro}\frac{\partial p_0}{\partial x}+\frac{1}{B^2}\frac{D^2}{H^2}\frac{\partial p_0}{\partial z}=0 \quad \text{along } (x,1). \tag{4.5}$$

Relation (4.1) can be solved subject to (4.2)–(4.5) by using Green's functions.

A typical result for a cosine-squared ridge (i.e. $h(x^*) = h\cos(\pi x^*/D)$) is sketched in figure 2 for the horizontal streamline pattern at mountaintop level (i.e. $z^*/h = 1.0$). Unlike the homogeneous case there is now an upstream influence with the streamlines deflecting to the left on approaching the ridge (left and right are defined as the directions when facing downstream). Fluid parcels reach their maximum leftward excursion before reaching the

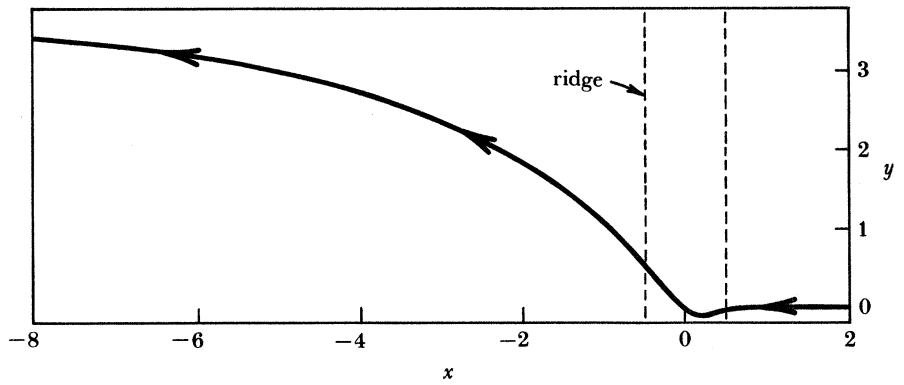

FIGURE 2. Streamline at mountaintop level for analytical model: $Ro = 0.05$, $E = 1.5\times10^{-4}$, $B = 0.81$, $h/H = 0.12$, $h/D = 0.11$ and $z^*/h = 1.0$.

mountain crest and then begin a long rightward drift reaching an asymptote far downstream with a permanent shift to the right of their upstream paths. This finite streamline displacement is due to Ekman suction; in the inviscid case the net streamline displacement is infinite in both the rigid lid case (Merkine 1975) and in the infinite depth case (equation 32 in Pierrehumbert 1984).

It is instructive to characterize changes in the predicted flow patterns as a function of the various system parameters. To this end we fix the geometrical parameters $h/D = 0.12$ and $H/D = 0.81$ at the values to be used in the experiments. We further consider solutions for various parameter combinations in the following ranges (again similar to the experiments): $0.05 \leqslant Ro \leqslant 0.30$; $1.0\times10^{-4} \leqslant E \leqslant 4.0\times10^{-4}$; $1.0 \leqslant B \leqslant 4.0$; and $0.0 \leqslant z^*/h \leqslant 8.0$.

To discuss the nature of the flow in both theory and experiment it is convenient to define a number of observables as sketched in figure 3. The characteristic upstream distance to which the ridge significantly affects the free stream motion is denoted as $X_1 = X_1^*/D$. Because the streaklines asymptotically approach the x^*-axis upstream of the topography, X_1 is defined as follows. First the point at which a tangent to the streakline is at a 10° angle with the x^*-axis is located. The tangent is then drawn and the distance between the point of intersection of this line with the x^*-axis and the upstream edge of the ridge is defined as X_1^*. The quantity $Y_1 = Y_1^*/D$ is defined as the maximum leftward excursion of the streakline as it passes over the ridge. The quantity $Y_2 = Y_2^*/D$ is defined as the maximum rightward shift of the streakline. In the theory this is an asymptote but in the experiments Y_2 is taken as the maximum rightward deflection; downstream of this point, fluid parcels again drift to the left in the experiments.

PHILOSOPHICAL TRANSACTIONS OF THE ROYAL SOCIETY A MATHEMATICAL, PHYSICAL & ENGINEERING SCIENCES

$\delta = 1$; note that the Ekman number defined herein is one half that of Pedlosky's, hence the factor $\frac{1}{\sqrt{2}}$ in the last term on the right hand side of our (2.31). The laboratory model has a rigid lid for which the boundary condition is given by (2.32). This, of course, is not the precise condition for either the ocean or the atmosphere. For low Rossby number flows Pierrehumbert (1984) shows that the characteristic depth scale of the response due to the bottom topography is restricted to vertical length scales of order fD/N. Thus if $fD/N \leqslant H$ the upper boundary will not have an important effect on the motion in the atmosphere, ocean or laboratory.

In oceanographic flows one is also interested in simulating the wind stress curl exerted at the ocean surface. Pedlosky's relation (6.9.14) for the ocean surface boundary condition includes this contribution. Such effects can be modelled in the laboratory but that is not a consideration in the present study.

Finally the present laboratory model satisfies the upstream, downstream and lateral boundary conditions as given by (2.28)–(2.30) respectively. Although these conditions are not the precise conditions satisfied in various atmospheric and oceanographic applications, their use is believed reasonable for obtaining the principle features of the flow field in the vicinity of the topographic features in question.

In summary, laboratory models of salt-stratified fluids can be used to a very good approximation to simulate large-scale motions as represented by the quasigeostrophic potential vorticity equations for the ocean and for the atmosphere, with the exception of its not being possible to simulate a non-Boussinesq term in the latter.

4. Infinite ridge model

Huppert & Stern (1974) showed that for the flow of a homogeneous rotating fluid over a long ridge in a channel, the sidewalls had an effect no matter what their separation distance. Nevertheless, the nature of the flow obtained by neglecting the sidewalls, especially in the vicinity of the ridge, is predicted reasonably by the infinite ridge approximation (see Boyer 1971). For later comparison with experiments, we thus briefly present the solution for the flow of a linearly stratified fluid over an infinite ridge.

Assuming a linear stratification, steady-state,† two-dimensionality, (i.e. $\partial/\partial y(\bar{v}) = 0$), $Ro \sim O(E^{\frac{1}{2}})$ and $h/H \sim O(Ro)$ (i.e. $\delta = 1$), the quasigeostrophic potential vorticity equation, (2.27) and boundary conditions (2.28), (2.29), (2.31) and (2.32) reduce, respectively, to

$$\frac{\partial^2 p_0}{\partial x^2} + \frac{1}{B^2}\frac{D^2}{H^2}\frac{\partial^2 p_0}{\partial z^2} = 0, \tag{4.1}$$

$$\partial p_0/\partial y = 1, \quad x \to \infty, \tag{4.2}$$

$$\partial p_0/\partial x = 0, \quad x \to -\infty, \tag{4.3}$$

$$\frac{E^{\frac{1}{2}}}{\sqrt{2}\,Ro}\frac{\partial p_0}{\partial x} - \frac{1}{B^2}\frac{D^2}{H^2}\frac{\partial p_0}{\partial z} = h_0 \quad \text{along } (x, 0), \tag{4.4}$$

† It is noted that in the experiments the Ekman boundary layers on the belt are fully established by the time the topography translates half way through the channel. Furthermore, analysis of the photographs indicates that steady-state conditions are realized in the interior for the second half of the topography traverse so that steady conditions are attained.

PHILOSOPHICAL TRANSACTIONS OF THE ROYAL SOCIETY A MATHEMATICAL, PHYSICAL & ENGINEERING SCIENCES

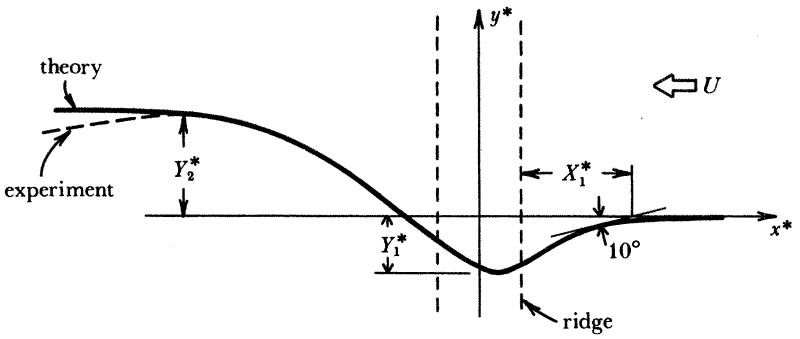

FIGURE 3. Definition of observables in analytical model and laboratory experiments (see text).

Rather than giving detailed plots of the theoretical flow patterns for specific values of the dimensionless parameters we present here the general behaviour of the above flow characteristics for the parameter ranges noted. Figure 4*a–d* shows schematic diagrams depicting the general behaviour of X_1, Y_1 and Y_2 for variations in Ro, E, B and z^*/h, respectively; in each diagram the parameters not indicated on the abscissa are held fixed. Figure 4*a*, for example, indicates that for fixed E, B, and z^*/h, Y_2 is independent of Ro, while X_1 and Y_1, both of which are substantially smaller in magnitude than Y_2, decrease with increasing Ro.

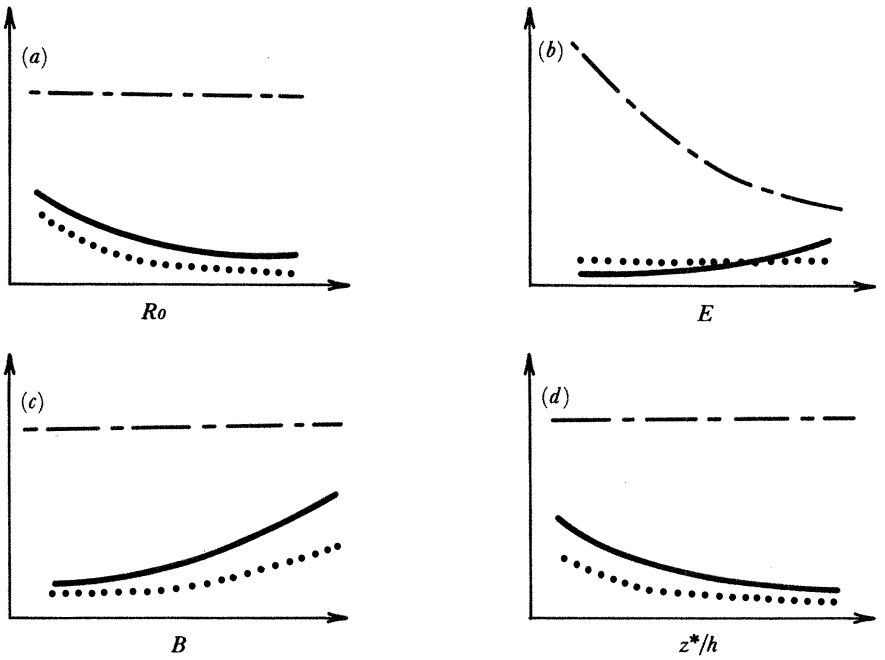

FIGURE 4. Qualitative dependence of flow characteristics for analytical model (see text). Solid line, X_1; dotted line, Y_1; dot–dashed line, Y_2.

As will be seen below, the infinite ridge theory does not give good quantitative predictions for X_1, Y_1 and Y_2 for the range of parameters considered in the experiments. We conclude that the principal reason for this poor agreement is the existence of the channel sidewalls. Presumably a theory along the lines of Huppert & Stern's (1974) analysis for the homogeneous

case is needed to predict the flow field adequately for the relatively narrow channel used in the experiments. It is expected that the present theory would give improved predictions for wider channels.

5. Experimental apparatus and techniques

The experimental apparatus is the same as that described in Kmetz (1982) and Boyer & Kmetz (1983) and thus only a brief description is given here. The basic facility is a rotating tow-tank 2.4 m long × 43 cm wide × 30 cm high. In the present experiments the tank is filled while at rest with a linearly stratified salt solution by using a now standard technique described by Oster (1965). The fluid is confined from above by a horizontal Plexiglas surface. This eliminates free surface motions that would otherwise occur owing to 'wind' shear stresses and inertial waves resulting from slight misalignment of the rotation and gravity vectors. A flexible belt covers the entire bottom of the tank and can be translated at a range of speeds in either direction along the channel axis. Topographic features are mounted on and translated with the belt.

After filling the tank the system is brought to solid body rotation by gradually increasing the angular velocity. Great care must be taken in this process so as not to destroy the density gradient. After approximately 2 h residual motions in the tank will have disappeared and the linearly stratified fluid is in solid body rotation. The topography is then translated at constant speed through the tank and observations are made relative to an observer moving with the topographic feature. This is accomplished by mounting a video camera and a 35 mm camera on a towing carriage that moves synchronously with the belt.

It is noted that the Ekman boundary layers on the translating belt transport 'heavy' fluid in both the downstream and rightward directions with respect to an observer moving with the belt. These transports set up secondary flows in the channel that are small compared with the primary flow past the ridge.

We use both the electrolytic precipitation technique described by Honji *et al.* (1980) and neutrally buoyant, spherical, polystyrene particles for flow visualization. In both of these techniques a plane of light (vertical for side views and horizontal for plan views), approximately 5 mm in width, is directed through the flow field of interest. The cameras are mounted in a direction perpendicular to the flow and streak photographs are taken of the light reflected from the tracer particles. The electrolytic precipitation technique provides streaklines (streamlines in steady flows) whereas the plastic particle method gives the approximate streamlines. The latter is especially important in the analysis of unsteady flows.

6. Experimental results

6.1. *General observations*

The initial experiments were addressed to obtaining a qualitative understanding of the effects of the various dimensionless parameters on the flow field. Figure 5, plate 1, presents a series of experiments in which a dye tracer is introduced at various levels, z^*/h, upstream of the ridge; in each of these runs the dimensionless parameters are held as close as possible to constant values.

The most striking observation is the decreased effect of the ridge in deflecting the streaklines as the height above the ridge increases. The upstream influence of the ridge is apparent at all levels for this set of parameters. Close inspection also indicates that the maximum leftward

(facing downstream) drift occurs upstream of the mountain crest with a somewhat weaker leftward turning of the streaklines on the upwind slope then rightward turning on the downwind slope. A rightward streakline shift at all levels far downstream of the ridge is also apparent. These observations are in qualitative agreement with the infinite ridge model.

The downstream horizontal streakline pattern also shows the evidence of lee waves (i.e. the shading and weak horizontal oscillations in the streaklines); this phenomenon, however, is better observed from the side-view observations discussed below. Note that the lee wave pattern is tilted somewhat from right to left. This is a sidewall effect caused by the leftward motion on the upwind side being blocked by the left wall, thus resulting in a somewhat faster streamwise flow on the left. Tracer particles have fallen to the lower Ekman layer on the upwind side of the experiment depicted in figure 5*d*; note that the leftward drift is at approximately 45° to the channel axis.

Figure 6, plate 2, presents a series of experiments in which a dye tracer is introduced at mountaintop level and for which all experimental parameters with the exception of the free stream speed are held fixed. The dimensionless parameters all are constant with the exception of *Ro* (and *Re*), which decreases from figure 6*a* to figure 6*c*. There is clearly a strong effect of Rossby number in this parameter range, with the streamlines being increasingly deflected in the vicinity of the ridge for decreasing *Ro*. Note that in figure 6*c* the downwind streakline slope is clearly stronger than the upwind slope.

Figure 7, plate 3, shows another series of experiments in which a dye tracer is released at mountaintop level. Here the only parameter varied is the stratification, $\Delta\rho/\rho_0$ (i.e. B), which is relatively weak in figure 7*a* and *b* and strong in figure 7*c*. For the strong stratification case the fluid velocities in both the streamwise and along-ridge directions in the vicinity of the mountaintop become substantially larger than the free stream. The downstream flow also tends to jet along the right wall of the channel. Sidewall effects are readily apparent in this case. The streakline irregularities in these examples are due to flow instabilities occurring near the right-hand wall. High B experiments such as that shown in figure 7*c* are accompanied by strong downslope winds that are better observed from side-view photographs; these observations are consistent with the theoretical results of Pierrehumbert & Wyman (1985, §6.1).

Lee wave motions can best be examined by viewing the streaklines from the side. Figures 8, 9, 11 and 12 (plates 4–7) all are taken with a vertically directed light sheet directed along the channel axis (i.e. $y^* = 0$). Figure 8 represents a series of experiments in which a dye tracer has been introduced at four levels (i.e. $z^*/h = 1.7, 3.2, 5.3$ and 7.2) and for which all parameters with the exception of the free stream speed are held fixed. From figure 8*a* to figure 8*c* the Rossby (and Reynolds) numbers thus increase. The bottom of the tank, including the topographic feature, is clearly visible from reflections of the vertically directed light beam. Moving vertically, the next four white lines originating at the white dots (solder wires) at the far right of the photographs are the streaklines, and the faint horizontal line above is the reflection from the upper bounding surface. As one notes for this series, with relatively weak stratification, the flow is smooth everywhere and the wave amplitude decreases as *Ro* decreases.

Below we shall categorize flows in terms of the mode of the vertical wave. We will use mode '0' to indicate cases in which there is no apparent lee wave, and mode n to indicate waves in which $\lambda_z = 2H/n$, where λ_z is the vertical wavelength. Figure 8*b*, *c* shows examples of mode 1, whereas figure 8*a* is one in which the amplitude is very small and the mode is difficult to observe.

A series of similar experiments at various stratification levels and no rotation are given in figure 9. The purpose of these non-rotating studies was to compare the results of the present tow-tank, in which the entire bottom is moving, with such classical studies as those of Long (1955) and Baines (1977) in which only the topography was moved. The results were gratifying in that qualitative comparisons with previous work were good.

Although the detailed shapes of the topographies used by Long (1955) differ from our cosine-squared ridge there is good agreement between the present results and his theoretical and experimental findings. Long used as his parameters the internal Froude number, $F_i = U/NH$, and the geometrical parameters $\beta = h/H$ and $b = D/2H$. Figure 10*a–d* shows the theoretical results given in his figures 7, 8, 11 and 10 respectively, and table 3 gives the parameter values for his results and our comparable experiments.

TABLE 3. PARAMETERS USED IN LONG'S (1955) THEORY AND PRESENT EXPERIMENTS

	Long (1955) theory				present experiments		
figure	F_i	$\beta = h/H$	$b = D/2H$	figure	F_i	$\beta = h/H$	$b = D/2H$
10*a*	0.25	0.15	0.4	9*a*	0.25	0.12	0.62
10*b*	0.20	0.20	1.0	9*b*	0.20	0.12	0.62
10*c*	0.083	0.12	0.4	9*c*	0.078	0.12	0.62
10*d*	0.091	0.09	0.4	11	0.069	0.12	0.62

Comparing figure 9*a* and figure 10*a* we note excellent qualitative agreement in spite of the fact that Long's topography was a bit higher and narrower. We note, for example, the location of the wave crest along the channel floor, which is well downstream of the mountaintop. The dye tracer along the bottom in all of the side-view photographs is due to 'heavy' tracer particles falling to the bottom in the vicinity of the tracer source and then moving along the belt floor during the experiment. Note that figure 9*a* represents a mode 1 case.

Figure 9*b* (mode 1) and figure 10*b* also compare favourably; note in particular the location of the first downstream wave crest near the channel floor, which is nearer the topography than in figure 9*a*. The comparison between figure 9*c* (mode 4) and figure 10*c* is also very good. For this lower F_i case the flow separates in the lee of the topographic feature. The detailed agreement between Long's theoretical prediction and the experiment is quite remarkable.

Finally Long, in figure 10*d*, shows a standing '**S**' pattern in his predicted 'streamline' at a height of about $\frac{1}{3}H$ above the bottom surface and slightly downstream of the ridge crest; that pattern is nicely reproduced in the streakline pattern of figure 11 (mode 3), an experiment conducted for a similar set of parameters to those used by Long. It must be noted, however, that figure 11 does not represent a steady-state pattern. The streakline in the vicinity of the '**S**' continues to oscillate, with the central portion of the '**S**' continually varying from almost a vertical orientation to that shown in figure 11; i.e. for this set of parameters the flow is unsteady. In this context it is interesting to note that the **S**-shaped pattern in figure 10*d* is statically unstable.

The experiments shown in figure 12 indicate the change in flow character observed by holding all parameters fixed with the exception of the stratification. Figure 12*a* (mode 1) and figure 12*b* (mode 1) again represent smooth flows with no apparent separation on the downstream portion of the ridge. For sufficiently large stratification, as in figure 12*c* (mode 3), separation occurs. Note, however, that separation is difficult to observe for streaklines

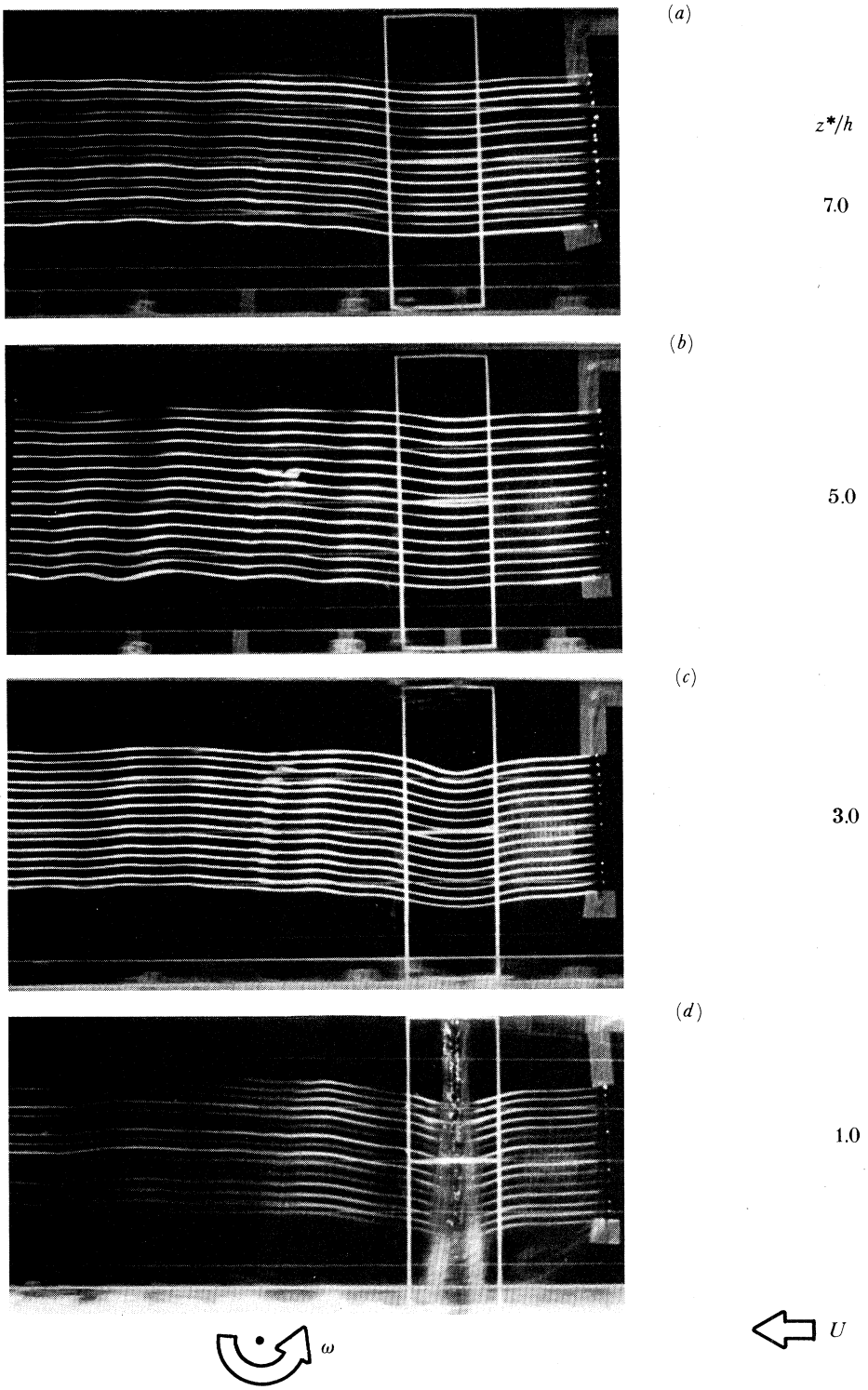

FIGURE 5. Vertical structure for fixed rotation, stratification (weak) and free stream speed: $Ro = 0.15$, $E = 1.5 \times 10^{-4}$ ($Re = 1540$), $B = 0.82$ ($\Delta\rho/\rho_0 = 5.6 \times 10^{-3}$), $h/H = 0.13$, $h/D = 0.11$ and $D/L = 0.32$.

(*Facing p.* 426)

PHILOSOPHICAL TRANSACTIONS OF THE ROYAL SOCIETY A MATHEMATICAL, PHYSICAL & ENGINEERING SCIENCES

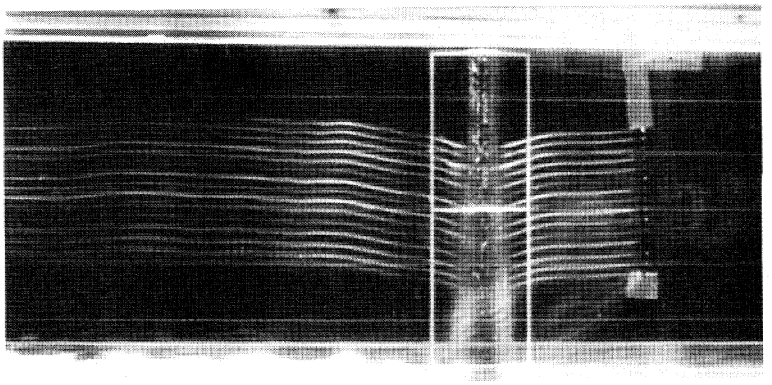

(*a*)

Ro	*Re*
0.15	1510

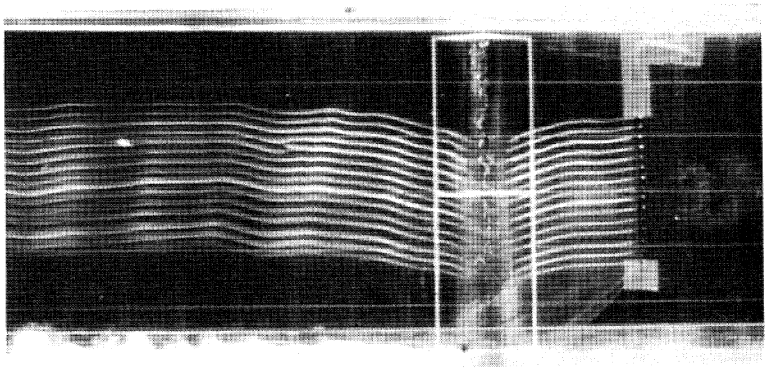

(*b*)

Ro	*Re*
0.10	1010

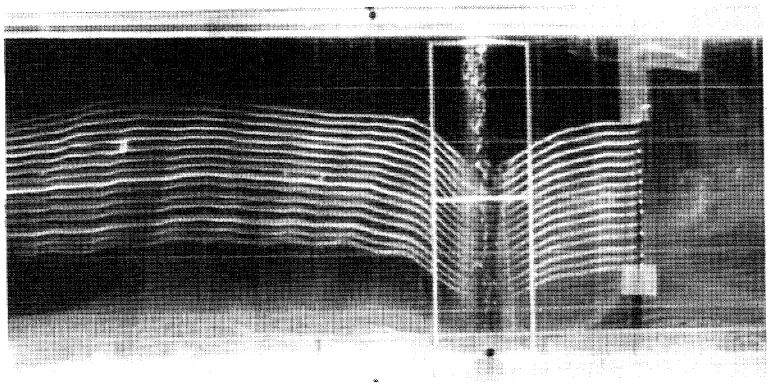

(*c*)

Ro	*Re*
0.05	500

FIGURE 6. Free stream speed effects for fixed rotation and stratification (weak) as observed at ridge crest level: $z^*/h = 1.0$, $E = 1.5 \times 10^{-4}$, $B = 0.81$ $(\Delta\rho/\rho_0 = 5.4 \times 10^{-3})$, $h/H = 0.13$, $h/D = 0.11$ and $D/L = 0.32$. The horizontal line along the ridge centre is a marker on the ridge indicating the centreline of the channel.

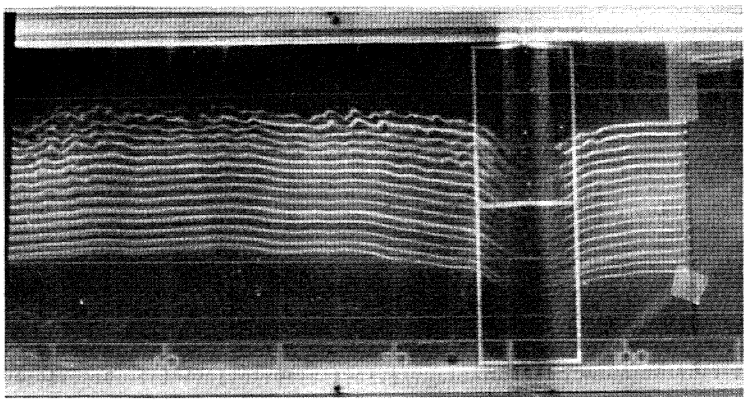

(*a*)

$\Delta\rho/\rho_0$ B

3.6×10^{-3} 1.33

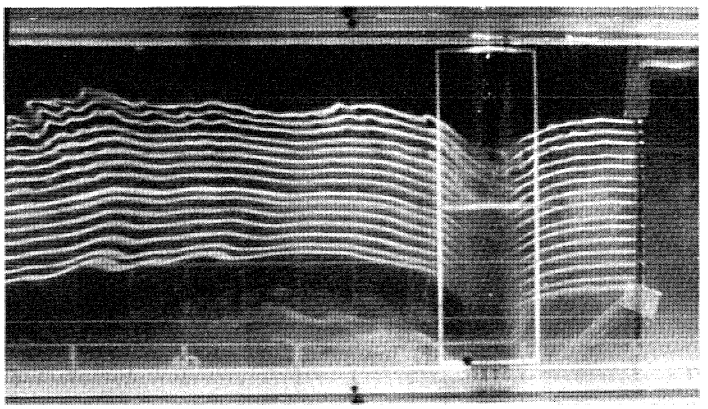

(*b*)

6.1×10^{-3} 1.71

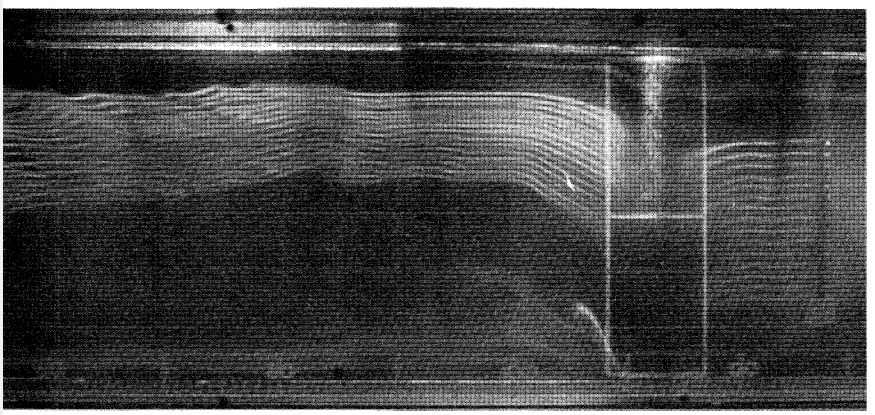

(*c*)

4.2×10^{-2} 4.49

FIGURE 7. Stratification effects for fixed rotation and free stream speed as observed at ridge crest level: $z^*/h = 1.0$, $Ro = 0.10$, $E = 3.0\times10^{-4}$ ($Re = 510$), $h/H = 0.13$, $h/D = 0.11$ and $D/L = 0.32$.

PHILOSOPHICAL TRANSACTIONS OF THE ROYAL SOCIETY A MATHEMATICAL, PHYSICAL & ENGINEERING SCIENCES

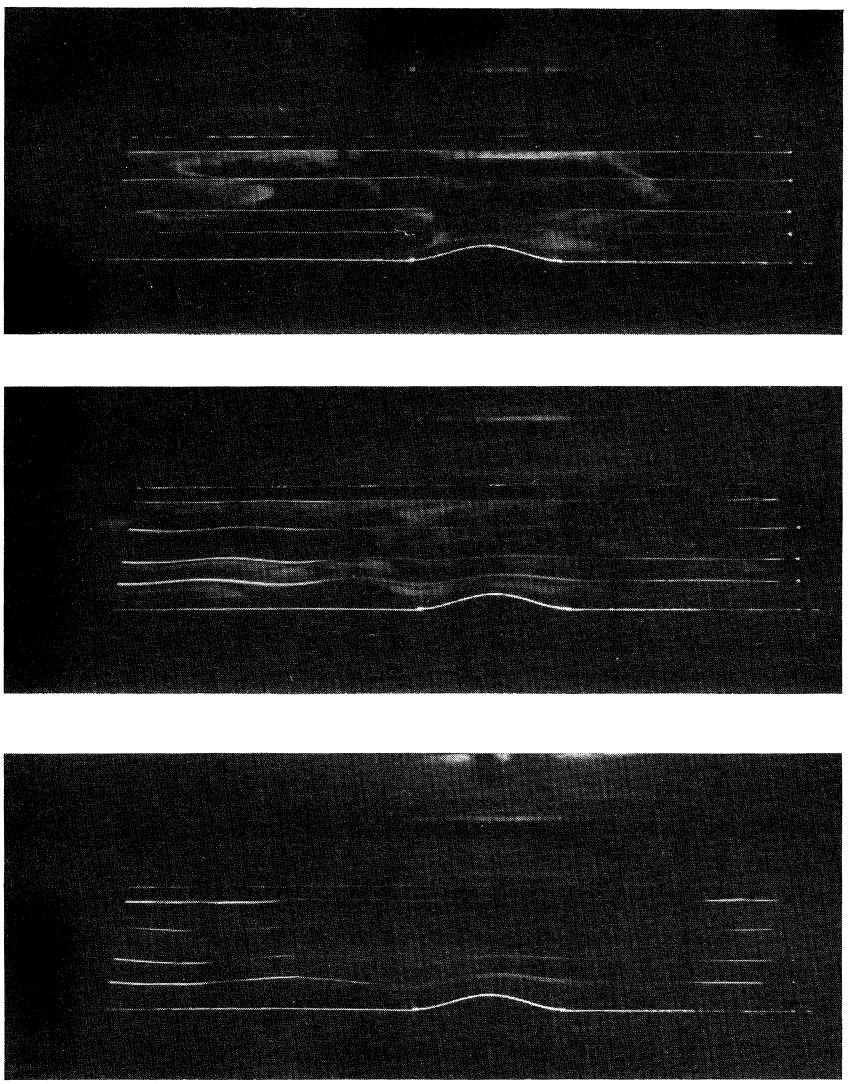

FIGURE 8. Free stream speed effects on lee wave structure for fixed rotation and stratification (weak): $E = 3.0 \times 10^{-4}$, $B = 1.33$ ($\Delta\rho/\rho_0 = 3.7 \times 10^{-3}$), $h/H = 0.13$, $h/D = 0.11$, $D/L = 0.32$ and $z^*/h = 1.7$, 3.2, 5.3 and 7.2. The white clouds in (*a*) and (*b*) are due to residual dye tracer from previous experiments and from dye tracer particles slightly heavier than the fluid medium 'dropping out' of the main streakline.

PHILOSOPHICAL TRANSACTIONS OF THE ROYAL SOCIETY A MATHEMATICAL, PHYSICAL & ENGINEERING SCIENCES

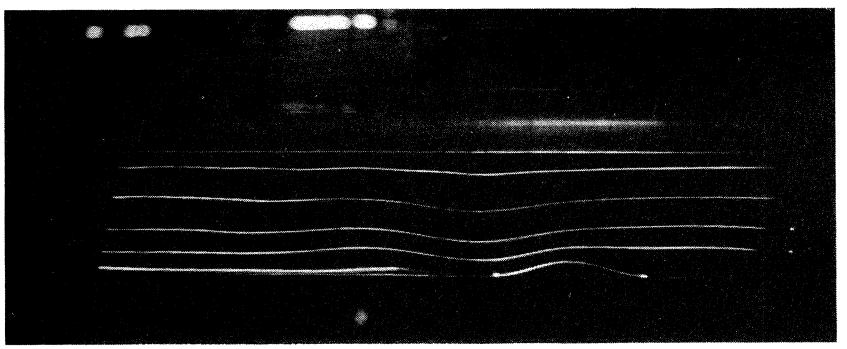

(*a*)

$\Delta\rho/\rho_0$

4.6×10^{-3}

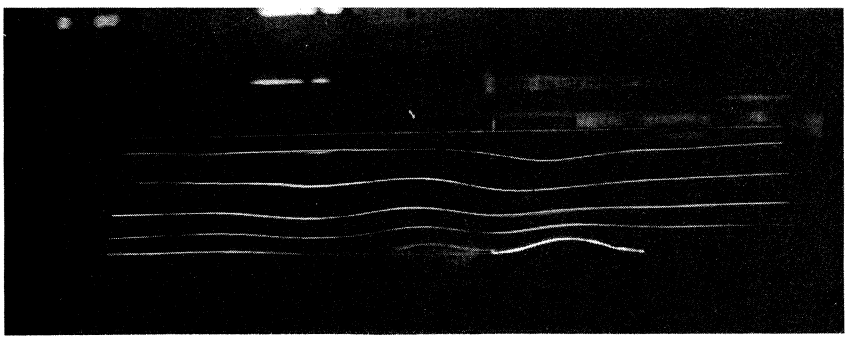

(*b*)

7.4×10^{-3}

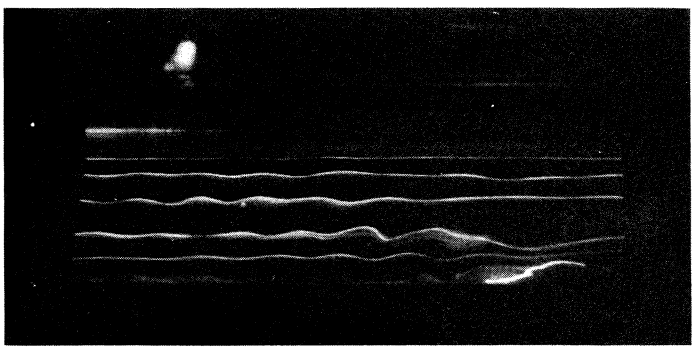

(*c*)

4.7×10^{-2}

U

FIGURE 9. Stratification effects on lee wave structure for zero rotation and fixed free stream speed: $Re = 510$, $h/H = 0.13$, $h/D = 0.11$ and $z^*/h = 1.7$, 3.2, 5.3 and 7.2.

PHILOSOPHICAL TRANSACTIONS OF THE ROYAL SOCIETY A MATHEMATICAL, PHYSICAL & ENGINEERING SCIENCES

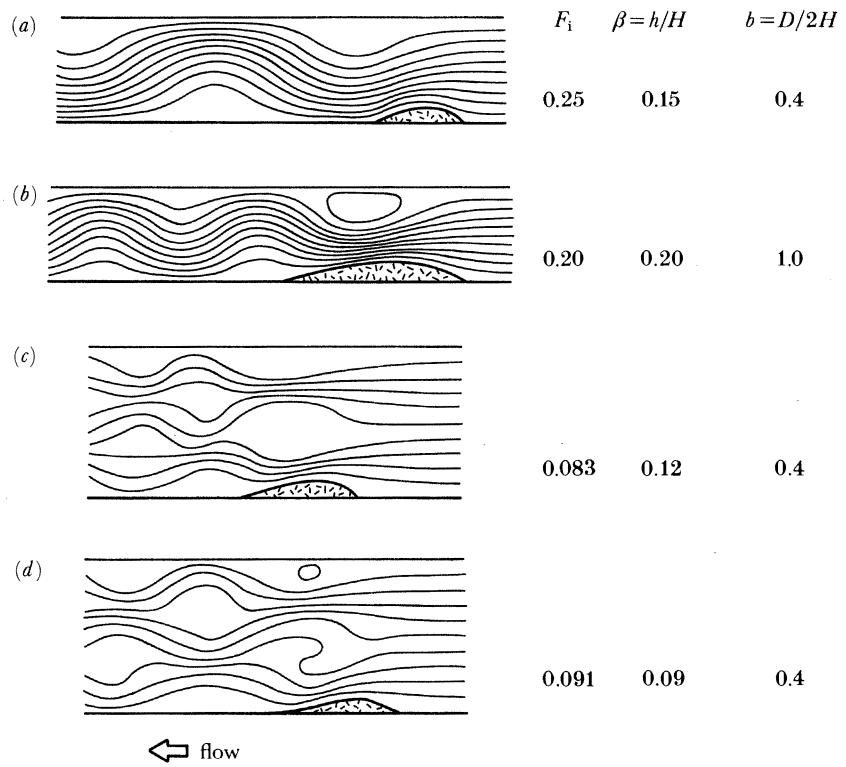

FIGURE 10. Theoretical streamline pattern for non-rotating flow based on Long's (1955) model. (Reprinted, with permission, from *Tellus*.)

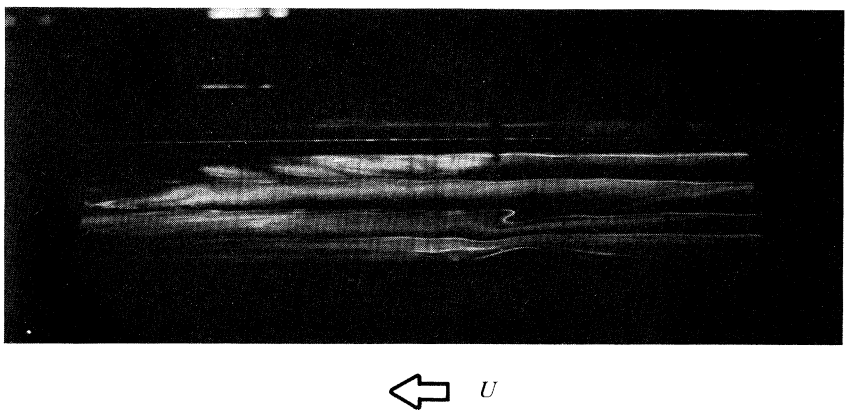

FIGURE 11. S-shaped streakline for unsteady non-rotating flow: $Re = 500$, $F_i = 0.069$ $(\Delta\rho/\rho_0 = 6.5 \times 10^{-3})$, $h/H = 0.13$, $h/D = 0.11$ and $z^*/h = 1.7$, 3.2, 5.3 and 7.2. See caption of figure 8 concerning white clouds in photograph.

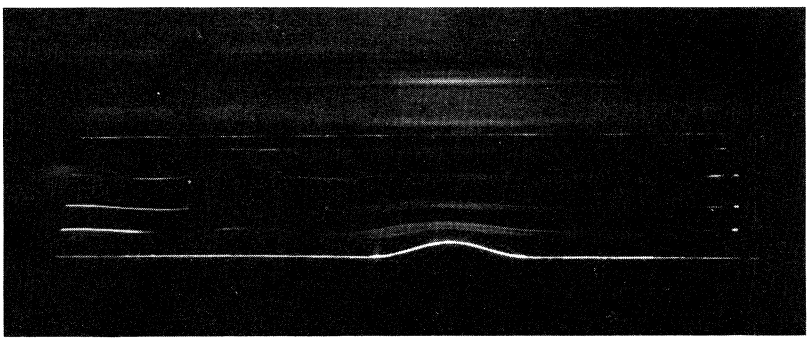

(*a*)

$\Delta\rho/\rho_0$ B

3.9×10^{-3} 0.68

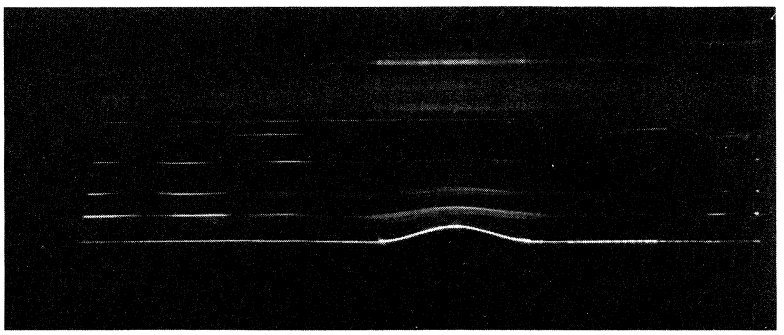

(*b*)

6.1×10^{-3} 0.86

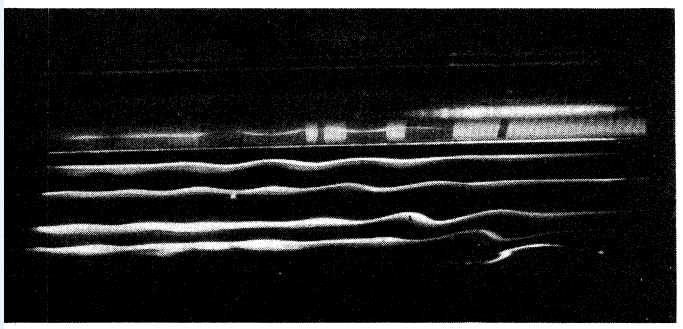

(*c*)

4.3×10^{-2} 2.28

FIGURE 12. Stratification effects on lee wave structure for fixed rotation and free stream speed: $Ro = 0.15$, $E = 1.5\times10^{-4}$ ($Re = 1510$), $h/H = 0.13$, $h/D = 0.11$, $D/L = 0.32$ and $z^*/h = 1.7$, 3.2, 5.3 and 7.2.

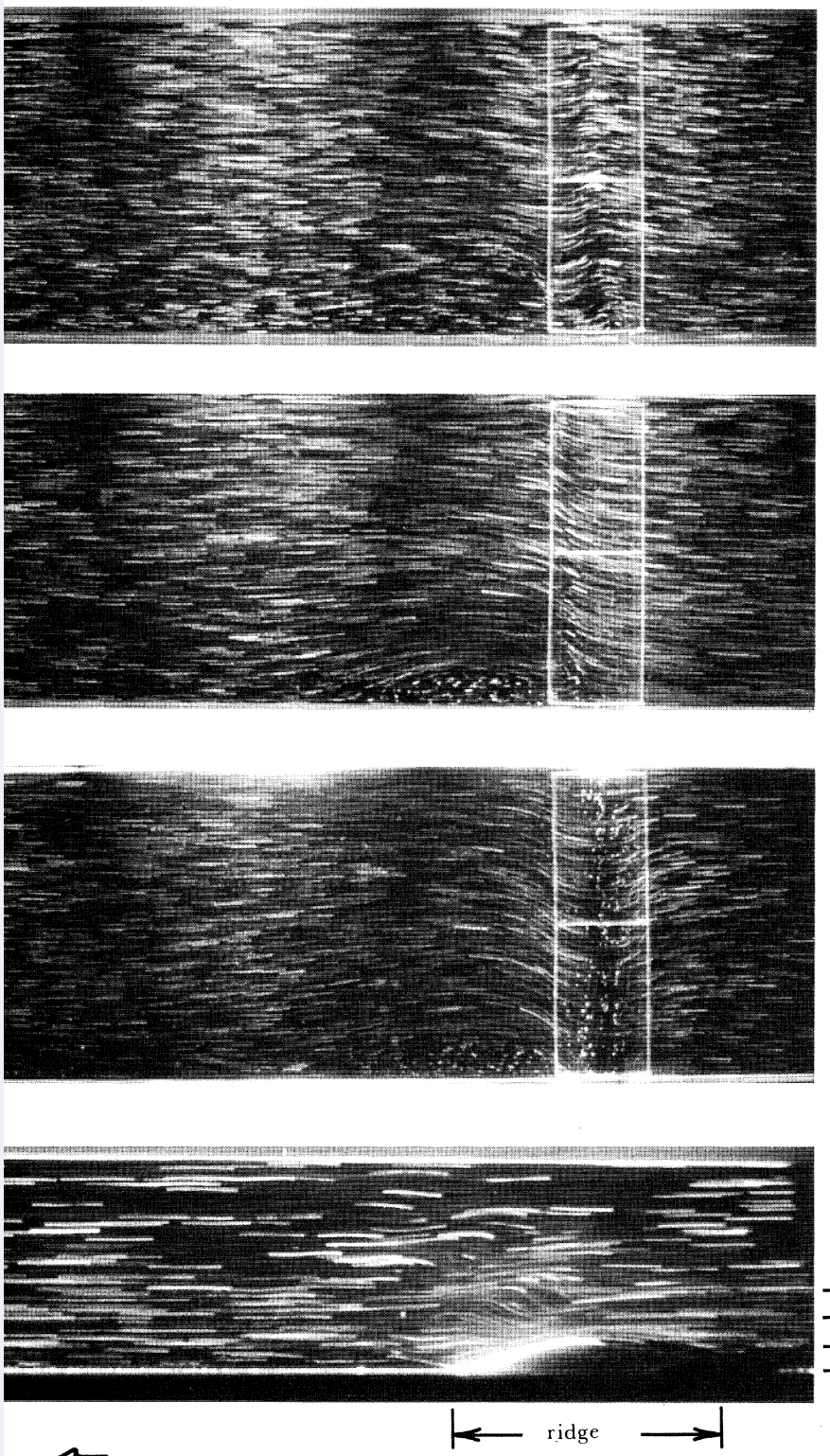

view	z^*/h
plan	3.0
plan	2.0
plan	1.0
side	–

FIGURE 13. Particle streak photographs of horizontal patterns at levels $z^*/h = 3.0$, 2.0 and 1.0 (i.e. (*a*), (*b*), (*c*) respectively) and vertical mode 5 pattern at $y^*/D = 0.0$ (i.e. (*d*)); $Ro = 0.25$, $E = 8.2 \times 10^{-4}$ ($Re = 470$), $B = 6.3$ ($\Delta\rho/\rho_0 = 1.1 \times 10^{-2}$), $h/H = 0.13$, $h/D = 0.11$, $D/L = 0.32$. Note that the horizontal scale in (*d*) is three times that in (*a*), (*b*) and (*c*).

originating in the fluid interior. The dark portions of the streaklines downstream of the ridge in figure 12*a* and figure 12*b* are caused by horizontal excursions of the lee wave pattern taking the streakline momentarily outside of the light sheet. Lee wave motions of this type are filtered out by the quasigeostrophic approximation used in deriving (4.1)–(4.5).

6.2. *Quantitative measurements*

6.2.1. *Flow régime diagram based on vertical wave structure*

The initial effort to analyse the data quantitatively was addressed to obtaining a régime diagram indicating regions of parameter space for which similar characteristic flow patterns could be observed. Various candidate observables were considered with the conclusion that a quite distinct one, and one that could be measured objectively, is the mode of the vertical wave structure, i.e. mode 0 being no lee waves, and mode n ($n = 1, 2, \ldots$) being the structure for which $\lambda_z = 2H/n$, where λ_z is the vertical wavelength. One difficulty with this measure is that observations become very difficult at small Rossby numbers because the wave amplitudes become exceedingly small. A further difficulty was that a great amount of lee wave data had been taken using four continuous streaklines in the vertical (e.g. figures 8, 9, 11 and 12) and that these data were difficult to analyse for high wave modes, say $n \geqslant 3$.

To solve this latter difficulty, a series of experiments were conducted with neutrally buoyant, polystyrene beads, of density $\rho \approx 1.04$ g cm^{-3} and typical diameter $d \approx 0.5$ mm, as tracer particles. These particles could, of course, only be used for weak density gradients whose mean density was very close to that of the beads. Streak photography, with the light sheet described above, was used to determine particle paths and thus, for sufficiently short time exposures, the streamline fields; note that for steady flows the exposure time is not critical in this regard.

Figure 13*a–c*, plate 8, shows photographs of the horizontal motion field at the elevations $z^*/h = 3.0$, 2.0 and 1.0, respectively. Figure 13*d* (wave mode 5) is a photograph of the vertical structure at $y^* = 0.0$. The exposure time for all of these experiments was 6 s. Note that the mountaintop observations in figure 13*c* indicate the occurrence of a barrier wind whereas this effect is not observed at higher levels (i.e. $z^*/h = 2.0$ and 3.0). Furthermore we note a clear difficulty related to the assumption of an infinite ridge because a separation bubble has occurred downstream and on the left side of the topographic feature. This bubble was noted to grow in length, breadth and height during the experiment. The separation bubble is also evident at $z^*/h = 2.0$ and to a lesser extent at $z^*/h = 3.0$. Note also the return to an approximately uniform free stream at large distances from the ridge in figure 13*a–c*. The 'zig-zag' nature of the horizontal flow pattern on the downwind side of the ridge at $z^*/h = 3.0$ (figure 13*a*) is related to the complex vertical structure at that height, as evidenced in figure 13*d*.

Photographs such as these can also be useful in determining the Eulerian velocity field, but for the present physical system for which the flow is fully three-dimensional, great care must be taken in interpreting the streaks because particles are continuously entering and leaving the light sheet. It must be noted that whereas particle photographs are more useful in determining the vertical wave-mode, wavelengths and wave amplitudes are more easily measured from continuous streakline photographs as obtained by the electrolytic precipitation technique.

For all of the experiments discussed in the present study, the geometrical parameters h/H, h/D and D/L were held fixed, so that only variations of B, Ro and E need be considered. Figure 14 is a Ro^{-1} against F_i régime map indicating the observed dominant vertical wave mode (number inside symbol) as a function of these parameters; Ekman number ranges are indicated

PHILOSOPHICAL TRANSACTIONS OF THE ROYAL SOCIETY A MATHEMATICAL, PHYSICAL & ENGINEERING SCIENCES

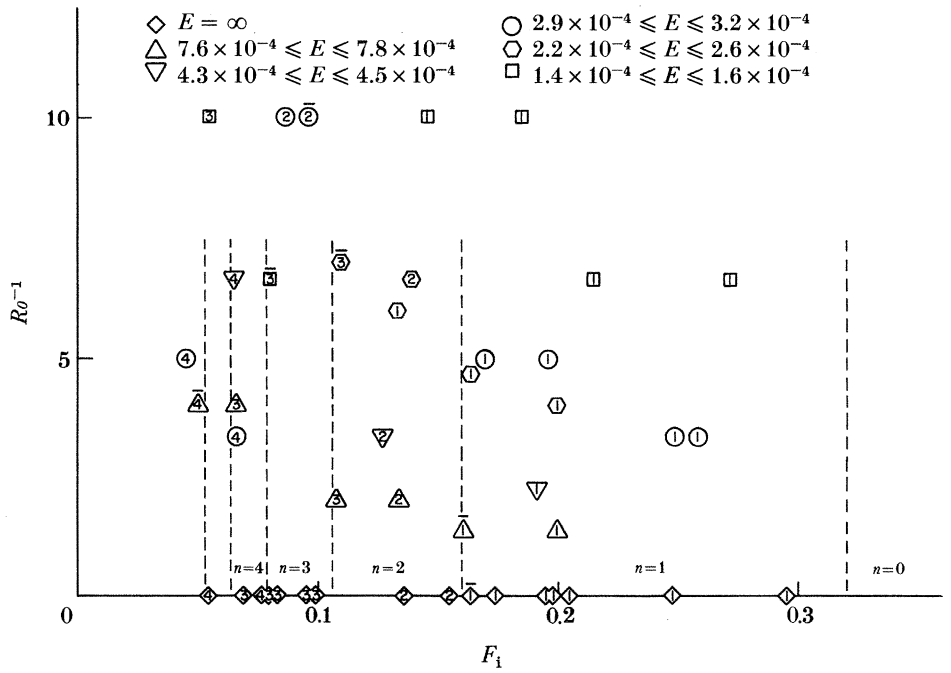

FIGURE 14. Flow régime map, Ro^{-1} against F_i, indicating locations in parameter space for which various vertical wave modes, n, are observed; different symbols refer to the Ekman numbers noted, the wave modes are indicated by the numbers inside the symbol, and the dashed lines represent the approximate divisions between the various flow régimes. Uncertain readings are indicated by an overbar.

by the various symbols as noted in the figure. It must be emphasized that in the rotating inviscid case there are infinitely many vertical modes present throughout parameter space; most of these have negligible amplitude.

Runs for which the vertical wave mode is not certain are indicated by an overbar. Because $E^{\frac{1}{2}} \ll Ro \ll 1$, it should be expected that Ekman suction, and hence E itself, should not be important in determining the general characteristics of the motion, including the vertical wave structure. It is apparent from figure 14 that the Ekman number is not an important determining factor, i.e. the mode of the vertical wave depends only on Ro^{-1} and F_i for fixed geometrical parameters. Following for example Long (1955) and Baines (1979), the ranges of F_i for which various vertical wave modes, n, should be observed for zero rotation (i.e. $Ro^{-1} = 0$) are indicated in figure 14. Note that, except for $n > 3$, all observations at zero rotation are in agreement with these theoretical predictions.

Although numerous experiments were conducted at $Ro^{-1} = 20$, the wave amplitudes in these cases were too small to make definitive judgments on the vertical wave mode. Even flows at $Ro^{-1} = 10$ (see, for example, figure 8*a*) were difficult to analyse for this same reason. We conclude from figure 14 that for the range of parameters of the present experiments and within the limits of our observations, the vertical wave mode is not greatly affected by rotation. The flow régime diagram is thus separated by the series of vertically oriented broken lines in figure 14, with the comment that these lines may veer gently to the left as rotation increases (i.e. as Ro^{-1} increases).

6.2.2. *Analyses of horizontal streakline patterns*

Photographs of the horizontal streakline patterns as given in figures 5–7 can be used to quantify various aspects of the flow. These measures can then be compared with the infinite ridge model and used to provide data for comparison with future models that account for sidewall effects. In analysing horizontal flow patterns we focus on the streakline whose upstream location is nearest the centre of the channel. For this streakline we then define X_1, Y_1 and Y_2 as sketched in figure 3 and as discussed in §4, where we again note that Y_2 is the maximum rightward excursion (i.e. not an asymptote, as for the theory).

In the terminology of meteorology, the quantity Y_1 can be considered as representative of the strength of the 'ridge' caused by the topographic feature; i.e. large Y_1 are related to regions of strong anticyclonic curvature. Figure 15 is a plot of Y_1 against Ro for a series of experiments in which the tracer is introduced at mountaintop level, $z^*/h = 1.0$; the streakline, of course,

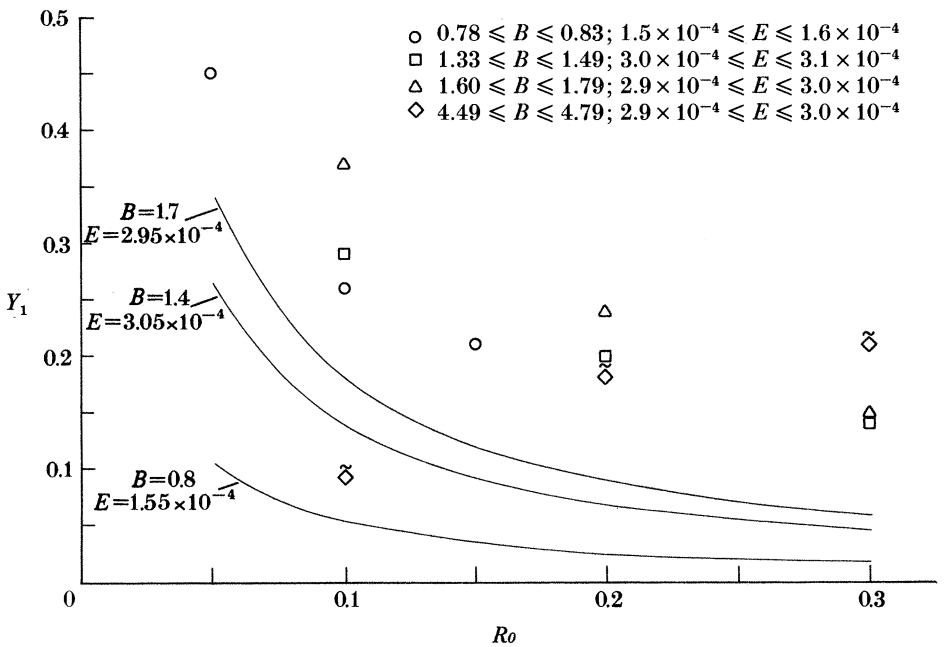

FIGURE 15. Plot of measured values of maximum leftward excursion of centre of streakline, Y_1 against Ro for various B and E and $z^*/h = 1$. Thin solid lines represent infinite-ridge model predictions for two B, E combinations and $z^*/h = 1$.

rises above this level in passing over the topography. Note that B and E are held approximately fixed for the various series of experiments at variable Ro. The variations in B are due to changes in the density stratification from one experiment to the next, while the variations in E are due to differences in the kinematic viscosity resulting from temperature fluctuations in the laboratory.

The data for the three lowest values of B in figure 15 show a clear decrease in Y_1 with increasing Ro, in qualitative agreement with the theory of §4 (see figure 4*a*). For these values of B and at fixed Ro, Y_1 tends to increase with increasing B. Assuming, as indicated by the theory for this parameter range (see figure 4*b*), that Y_1 is independent of E, this result is also in qualitative agreement with the theory (see figure 4*c*). Note, however, that for the largest value

PHILOSOPHICAL TRANSACTIONS OF THE ROYAL SOCIETY A MATHEMATICAL, PHYSICAL & ENGINEERING SCIENCES

of $B \approx 4.6$, the leftward excursion at certain of the lower values of Ro becomes substantially smaller than for the lower values of B. A closer examination of these experiments indicates flows with large streamwise and along-mountain velocity components in the vicinity of the mountaintop and some flow separation in the lee. Because such flow characteristics are not included in the theoretical model, the experiments are not even in qualitative agreement with the theory. Examples of flows with large B are given in figures 7*c* and 12*c*. In figure 15 and in subsequent plots a tilde (˜) is placed above the symbol to indicate a separated flow with high B.

We have also plotted as light solid lines on figure 15 the predictions for Y_1 from the infinite ridge model for the three lowest values of B. It is noted that although the qualitative shape of the curves and their relative locations are in good agreement with experiment, the theory seriously underestimates Y_1.

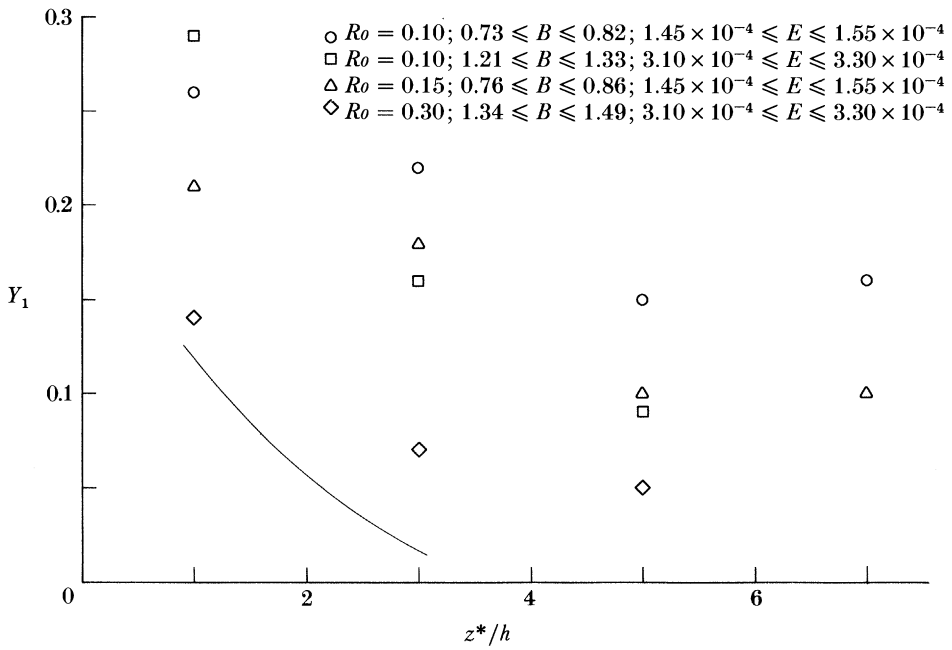

FIGURE 16. Plot of measured values of Y_1 against z^*/h for various combinations of Ro, B and E. The thin solid line represents infinite-ridge model predictions for $Ro = 0.10$, $E = 3.2 \times 10^{-4}$ and $B = 1.27$.

Figure 16 shows how the maximum leftward deflection Y_1 varies with the elevation, z^*/h, for various combinations of Ro, B and E. For all parameter combinations Y_1 decreases with elevation. This behaviour agrees qualitatively with the infinite ridge model (see figure 4*c*) and with the generally accepted notion that stratification inhibits the effect of bottom topography at higher elevations. Examining the two series of experiments at fixed $Ro = 0.10$ and different B (i.e. $B \approx 0.78$ and $B \approx 1.27$), we note that the stronger stratification case tends to develop a sharper decay of topography effect with height. Note also that smaller Y_1 are obtained for larger Ro (i.e. compare $Ro = 0.10$ and $Ro = 0.15$) and approximately fixed B (i.e. $B \approx 0.8$) at all levels in the data of figure 16. A theoretical plot of Y_1 against z^*/h is also included as a light solid line on figure 16 for one Ro, B and E combination.

Figure 17 depicts the maximum rightward excursion, Y_2, as a function of Ro for various values of B and E. Focusing on the three lowest values of B, we note the relatively weak dependence of Y_2 on Ro (i.e. possibly a small decrease with increasing Ro) and essentially no dependence on B for fixed Ro. These observations are in qualitative agreement with the predictions of the infinite ridge model (i.e. see figure 4*a*, and figure 4*c*, respectively). For experiments at large B, the strong along-mountain velocity component develops large rightward displacements; see,

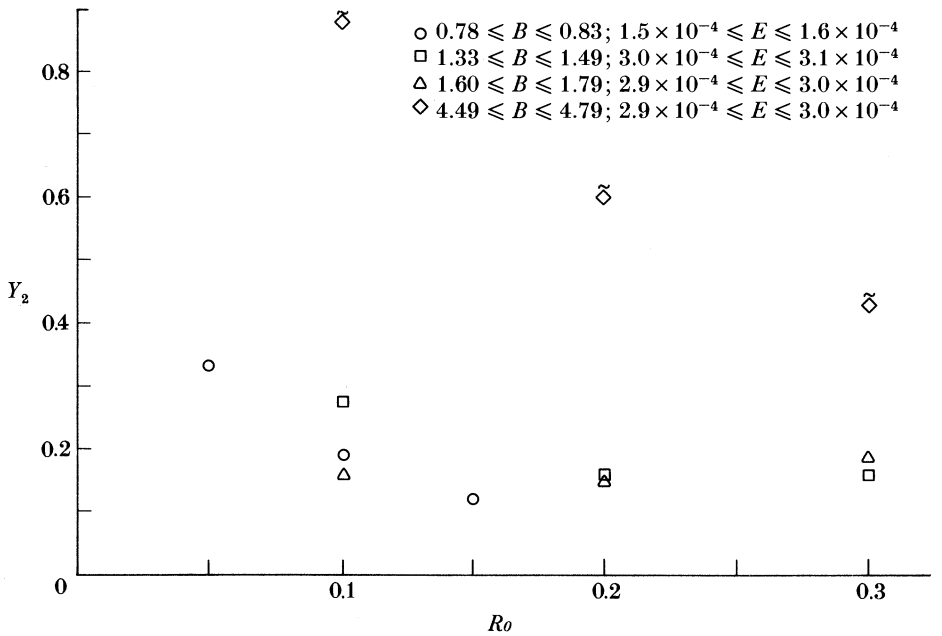

FIGURE 17. Plot of measured values of maximum rightward excursion of centre streakline, Y_2 against Ro for various B and E.

for example, the photograph in figure 7*c*. As noted in figure 4*a–d*, Y_2 depends only on the Ekman number, and, as seen in figure 2, the Y_2 asymptote is typically reached many ridge diameters downstream of the topography. The infinite ridge prediction for Y_2 for the cases where $E \approx 3 \times 10^{-4}$ in figure 17 is $Y_2 \approx 2.5$, almost an order of magnitude larger than these values observed. The sidewalls simply do not allow the long gradual rightward drift predicted in the theory.

A plot of Y_2 against z^*/h for various Ro, B and E combinations is given in figure 18. Within the accuracy of the measurements, Y_2 is in qualitative agreement with the infinite ridge model (i.e. see figure 4*d*). But again, sidewall constraints lead to serious overestimates by roughly an order of magnitude for these parameters. For fixed Ro (i.e. $Ro = 0.10$) and variable B (i.e. $B \approx 0.78$ and $B \approx 1.27$), Y_2 is slightly larger for larger B at all levels, whereas the theory suggests that Y_2 is independent of B (i.e. see figure 4*c*). Similarly for fixed B (i.e. $B \approx 0.78$) the deflection, Y_2, is greater for smaller Ro (i.e. compare $Ro = 0.10$ and $Ro = 0.15$) at all levels, whereas the theory suggests that Y_2 is independent of Ro (see figure 4*a*).

A quantity of considerable interest is the distance upstream of the topography to which there is substantial influence of the mountain on the curvature of the streamlines. We recall that for a homogeneous fluid and for infinitesimal topographies there is no upstream influence (see Boyer

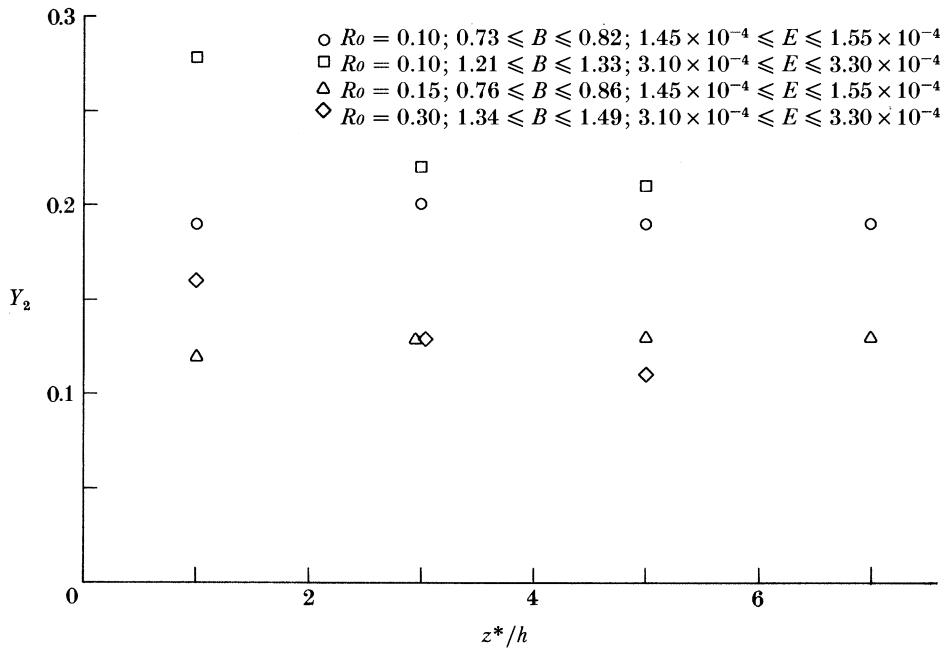

FIGURE 18. Plot of measured values of Y_2 against z^*/h for various combinations of Ro, B and E.

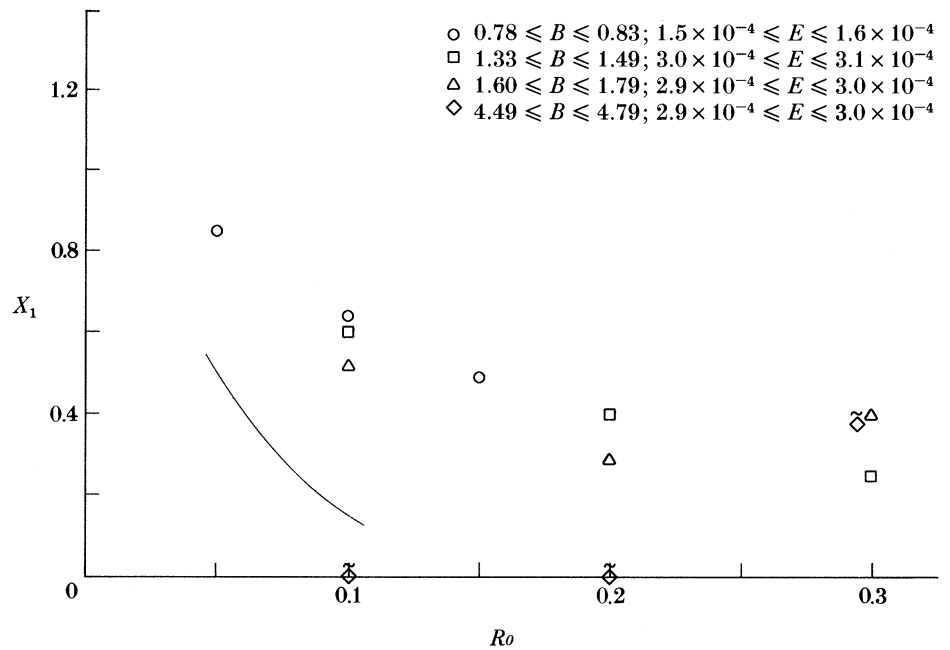

FIGURE 19. Plot of measured values of characteristic upstream influence distance of centre streakline, X_1 against Ro for various B and E. The thin solid line represents the infinite ridge model prediction for $B = 1.7$ and $E = 2.95 \times 10^{-4}$.

1971). Figure 19 is a plot of the upstream influence distance X_1 against Ro for various B and E combinations with all measurements made at mountaintop level, $z^*/h = 1.0$.

We note first that there is a general decrease in X_1 for an increase in Ro for the three lowest values of B, in qualitative agreement with the infinite ridge model (see figure 4*a*). The experiments at large B do not show this dependence. A theoretical prediction for one B and E combination is given as the thin solid line in figure 19, with the theory again being in qualitative agreement with the observations but seriously underestimating X_1. Note that for the range of parameters considered and for the three lowest values of B, X_1 is independent of B within the accuracy of the experimental observations.

Figure 20 depicts the dependence of X_1 on elevation, z^*/h. We note that at the lower levels, at least for the experiments of smaller Rossby numbers, X_1 may increase, or at least decrease

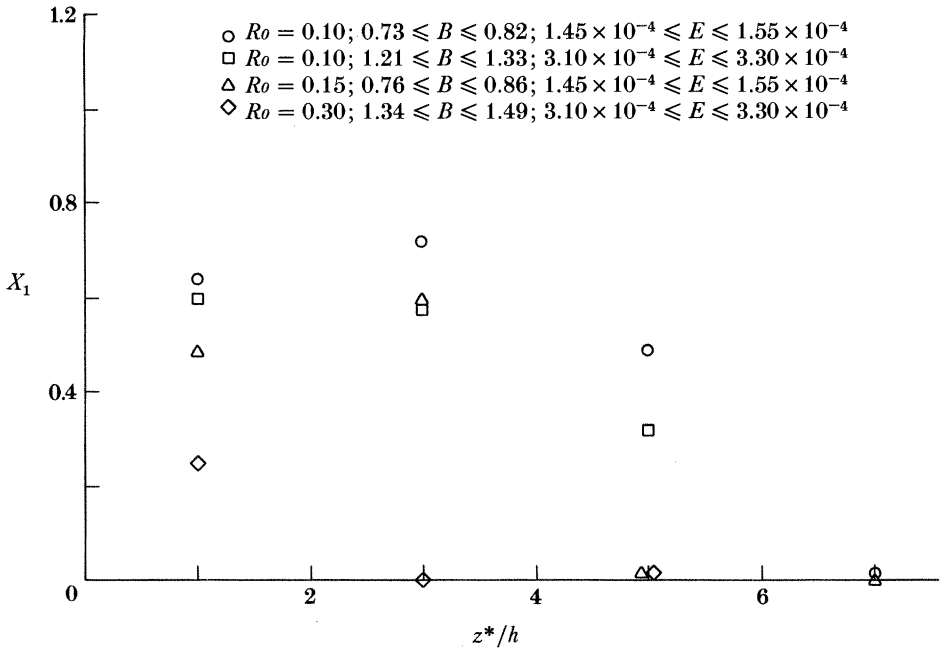

FIGURE 20. Plot of measured values of X_1 against z^*/h for various combinations of Ro, B and E.

very slowly with height. In the upper layers, as might be expected, X_1 drops rather sharply with elevation, in qualitative agreement with the infinite ridge model (see figure 4*d*). Note that for approximately fixed B (i.e. $B \approx 0.8$), X_1 is larger for smaller Ro (i.e. compare $Ro = 0.10$ and $Ro = 0.15$).

6.2.3. *Analysis of lee wave structure*

Side-view photographs as given in figures 8, 9, 11 and 12 can be used to quantify the observed wavelengths and wave amplitudes. A schematic diagram defining the observables is given in figure 21. Streaklines are depicted by introducing a dye tracer at the approximate levels $z_1 = z_1^*/h = 1.7$ and $z_2 = z_2^*/h = 3.2$ as noted. The normalized trough-to-trough wavelengths $\lambda_1 = \lambda_1^*/D$ and $\lambda_2 = \lambda_2^*/D$ are defined for the first wave downstream of the mountain crest for the two streaklines, respectively. Similarly we define the respective normalized wave amplitudes $a_1 = a_1^*/h$ and $a_2 = a_2^*/h$.

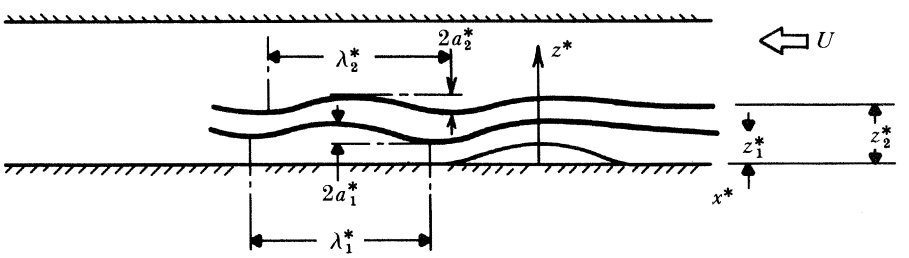

FIGURE 21. Definition of observables in analysing lee wave structure (see text): $z_1^* = 1.7$ cm; $z_2^* = 3.2$ cm.

Long (1955), Baines (1979), Castro (1983) and others give the theoretical lee-wavelength from linear theory for non-rotating flow as

$$\frac{\lambda^*}{D} = \frac{2H/D}{\{1/\pi^2 F_i^2 - n^2\}^{\frac{1}{2}}}, \tag{6.1}$$

where n is the vertical wave mode as discussed above. Figure 22 is a plot of λ^*/D against F_i for a non-rotating flow. The heaviest solid line represents the theoretical prediction for the relation for the first vertical wave mode, $n = 1$, and the two light solid lines for $n = 2$ and $n = 3$ respectively. Along the abscissa we note the expected vertical wave mode as a function of F_i. For example, for the $n = 1$ range, only that mode can be observed; for the $n = 2$ range both the first and second modes can occur; and so on.

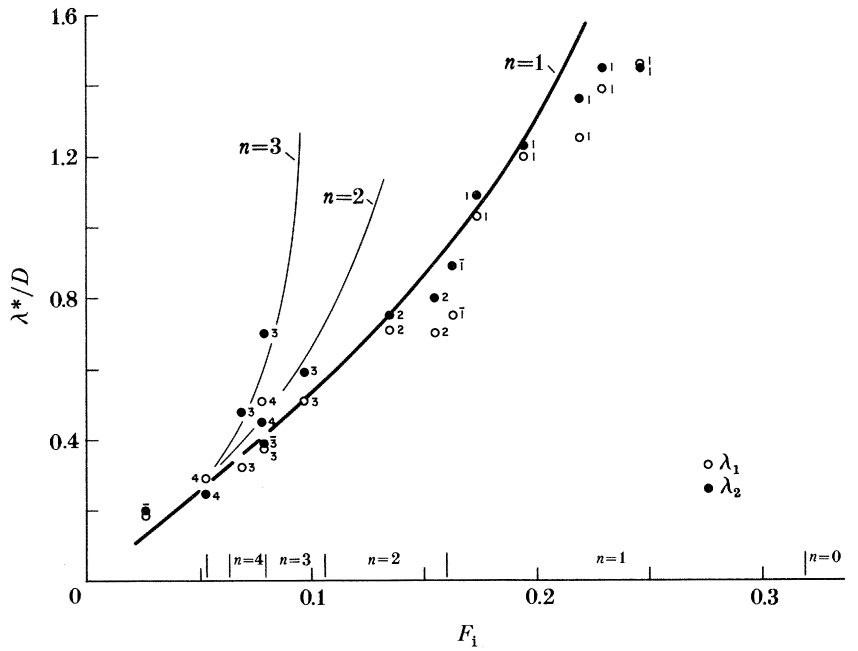

FIGURE 22. Plot of measured values of normalized horizontal wavelength λ^*/D, against F_i for non-rotating flow; open symbols, level 1, and closed symbols, level 2 (see figure 21 and text). Solid lines represent predictions from linear theory for vertical wave modes $n = 1$, 2 and 3. Numbers to the right of symbols represent observed wave mode. Expected vertical wave mode régimes are indicated as a function of F_i.

We note first that the wavelength at the upper level is consistently larger than that at the lower level. We also note reasonable agreement with theory with the experiments at larger F_i in the $n = 1$ mode showing consistently smaller wavelengths than those predicted. The agreement with theory is comparable with that given for example by Castro *et al.* (1983) and we conclude that the present facility in which the entire bottom translates with the topography can be used effectively for non-rotating experiments as well. In the non-rotating case, however, long runs may present difficulties owing to the growing boundary layer along the belt.

Although amplitude data were also taken for the non-rotating experiments, the data did not correlate well with the internal Froude number, F_i. Part of the reason is the difficulty of defining wave amplitudes for the complex flow patterns observed for wave modes greater than $n = 1$; see for example the downstream flow pattern obtained from Long's (1955) model in figure 10*c*, *d*. It is believed that the poor correlation for the mode $n = 1$ data was most probably caused by small vertical motions of the belt and the fact that measurements of amplitudes of only several millimetres were being made from dye traces of the order of 1 mm width. Let us now consider the influence of rotation on the wavelengths and wave amplitudes.

A theoretical prediction for the rigid lid horizontal wavelength in the rotating case can be obtained from Queney's (1947) analysis; see also relation (3.30) in Smith's (1979) review paper. We can write

$$\frac{\lambda^*}{D} = \frac{2\sqrt{2}(H/D)}{\left[\left\{\left(n^2 - \frac{1}{\pi^2 F_i^2}\right)^2 + \frac{4n^2}{\pi^2}\frac{H^2}{D^2}\frac{1}{Ro^2}\right\}^{\frac{1}{2}} - \left\{n^2 - \frac{1}{\pi^2 F_i^2}\right\}\right]^{\frac{1}{2}}}, \tag{6.2}$$

where we note that the vertical wavenumber $k_z = n/H$ has been used. Figure 23 is a plot of

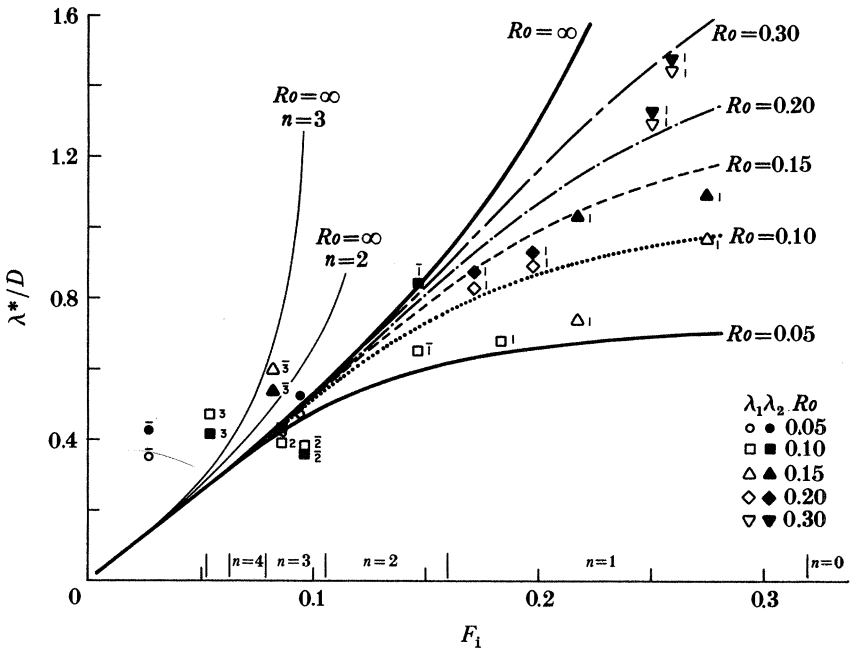

FIGURE 23. Plot of measured values of normalized horizontal wavelength, λ^*/D, against F_i for various Ro; open symbols, level 1, and closed symbols, level 2 (see figure 21 and text). Lines originating at the origin and terminating on the right represent predictions from linear theory for vertical wave mode $n = 1$. The thin solid lines on the left centre of diagram are for $Ro = \infty$ and vertical wave modes $n = 2$ and 3, respectively. Numbers to the right of symbols represent observed wave modes. Expected vertical wave mode régimes for $Ro = \infty$ are indicated as a function of F_i.

the normalized horizontal wavelength, λ^*/D, against F_i. Theoretical plots for mode 1 waves are shown for a series of Rossby numbers including $Ro = \infty$. Also plotted are the $Ro = \infty$ relations for the second and third modes where we note that the plot would simply become too 'busy' if Ro variations were also included for these modes.

We note again that for all of the mode 1 observations the upper wavelength is larger. While there are relatively few data points, we do note that the observed wavelengths tend to fall near the predictions of the rotating theory, i.e. the $Ro = \infty$ curve for fixed F_i predicts much larger wavelengths than those observed. In summary the Queney (1947) theory suggests decreased wavelengths for increased rotations at fixed F_i and our observations so indicate.

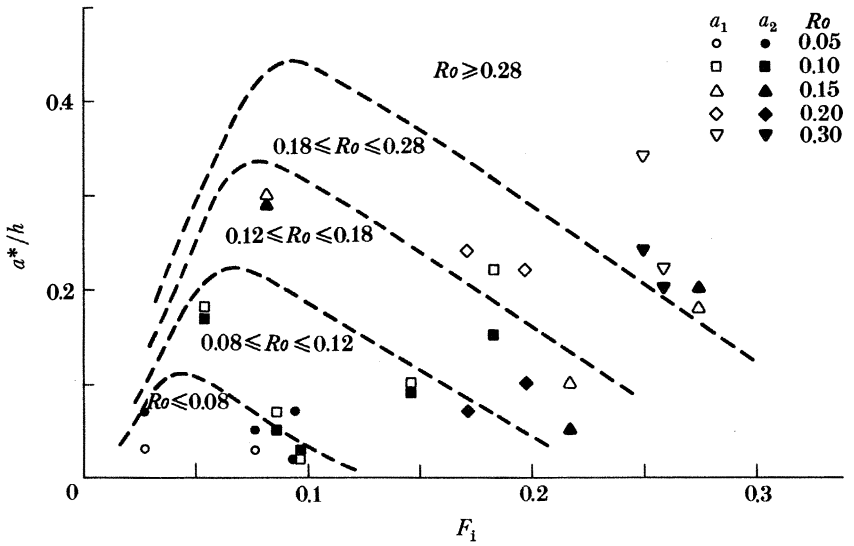

FIGURE 24. Plot of measured values of normalized wave amplitude, a^*/h, against F_i for various Ro; open symbols, level 1, and closed symbols, level 2 (see figure 21 and text). The dashed lines represent the approximate way in which the amplitudes vary with F_i and Ro.

Figure 24 is a plot of the normalized wave amplitude, a^*/h, against F_i for various values of Ro. Note that for the experiments at higher F_i the lower-level amplitude was consistently larger than that observed at the upper level. It is again noted that substantial errors are inherent in these data because of the very small amplitudes being observed. Nevertheless a consistent and interesting trend in the data is evident. For fixed F_i the wave amplitude decreases for decreasing Ro where we recall earlier qualitative observations on this point (i.e. see figure 8*a–c*). The broken lines on figure 24, separating regions of approximately equal Rossby numbers, must be considered a very rough estimate.

7. An atmospheric example and concluding remarks

Let us now consider a possible atmospheric simulation. The Sierra Nevada mountains investigated by Marwitz (1983) will be taken as a symmetric cosine-squared ridge as in the above experiments, although it must be recognized that the eastern or downwind portion is at a higher elevation than the western slopes. For the Sierra Nevadas we take $h_s = 2.5$ km, $H_s = 10$ km (height of tropopause), $D_s = 200$ km, $f_s = 10^{-4}$ s^{-1}, $U_s = 10$ m s^{-1},

$N_s = 1.1 \times 10^{-2}$ s^{-1} (from Marwitz (1983), stable case), and $\nu_s = 5$ m^2 s^{-1} (from Holton 1979), where the subscript s refers to the Sierras. These determine the dimensionless parameters as $(Ro)_s = 0.5$, $E_s = 5 \times 10^{-4}$, $B_s = 110$, $h_s/H_s = 0.25$, and $h_s/D_s = 1.25 \times 10^{-2}$.

We note that because $E_s^{\frac{1}{2}} \ll (Ro)_s$, Ekman suction is negligible. Recognizing that the non-Boussinesq term cannot be modelled in the laboratory (see §3), we then require for modelling the remaining terms in the quasigeostrophic potential vorticity equation (2.27) and boundary conditions (2.28)–(2.34) that

$$B_s H_s/D_s = B H/D \tag{7.1}$$

and

$$\frac{1}{Ro_s}\frac{h_s}{H_s} = \frac{1}{Ro}\frac{h}{H}. \tag{7.2}$$

Because $H/D = 0.81$ is fixed in the experiments, this requires from (7.1) and the above prototype values that $B = 6.8$. Similarly, because $h/H = 0.13$ is fixed, from (7.2) we require that $Ro = 0.25$. The series of horizontal particle streak photographs and the vertical cross section observations given in figure 13 approximately match these parameters. Note the strong barrier-wind effect at the lower levels and the fact that there is no 'southerly flow' in the upper levels. Note also the strong lee wave pattern. While such aspects of the real flow as vertical shear, nonlinearities in the stratification, and unsteadiness of the free stream are not modelled, the general nature of the flow seems to fit observations well.

The most severe problem continues to be the effect of the lateral bounding surfaces. This difficulty, of course, is related to our using a topography extending across the entire channel. Experiments are currently under way for isolated topographic features (e.g. the Rocky Mountains, Tibetan Plateau and Greenland). If such features are sufficiently far from the sidewalls, it appears that the effects of such lateral bounding surfaces are negligible.

In summary, a laboratory experiment has been developed that has good potential for modelling a wide range of oceanic and atmospheric motions. The particular geometry of a symmetric ridge extending across the channel has been extensively examined and the observations are in qualitative agreement with predictions from a quasigeostrophic potential vorticity model for an infinite ridge, although quantitative agreement is not good because of the existence of lateral bounding surfaces.

This study was supported by the Division of Atmospheric Sciences of the National Science Foundation under grant number ATM-8218488.

The authors thank the following individuals for their helpful discussions concerning various aspects of this work: Dr Peter A. Davies (University of Dundee, U.K.), Dr Hiroyuki Honji (Research Institute for Applied Mechanics, Kyushu University, Japan) and Dr Michael Foster (Ohio State University) (provided Green's function solutions for infinite ridge model), who were all colleagues and frequent visitors to our laboratory; Mr Ruirong Chen and Mrs Lijun-Tao, visiting scientists from the Academia Sinica, Beijing, China; and Dr Alan Hartley and Dr William Lindberg, Department of Mechanical Engineering, University of Wyoming. The authors also thank Mr Stephen Ownbey for his efforts in plotting the various data.

PHILOSOPHICAL TRANSACTIONS OF THE ROYAL SOCIETY A MATHEMATICAL, PHYSICAL & ENGINEERING SCIENCES

References

Baines, P. G. & Davies, P. A. 1980 Laboratory studies of topographic effects in rotating and/or stratified fluids. In *Orographic effects in planetary flows* (GARP Publications Series no. 23) (ed. R. Hide & P. W. White), pp. 233–299. Geneva: World Meteorological Organization.

Baines, P. G. 1977 Upstream influence and Long's model in stratified flows. *J. Fluid Mech.* **82**, 147–159.

Baines, P. G. 1979 Observations of stratified flow over two-dimensional obstacles in fluid of finite depth. *Tellus* **31**, 351–371.

Boyer, D. L. & Kmetz, M. L. 1983 Vortex shedding in rotating flows. *Geophys. astrophys. Fluid Dyn.* **26**, 51–83.

Boyer, D. L. 1971 Rotating flow over long shallow ridges. *Geophys. Fluid Dyn.* **2**m, 165–184.

Castro, I. P., Snyder, W. H. & Marsh, G. L. 1983 Stratified flow over three-dimensional ridges. *J. Fluid Mech.* **135**, 261–282.

Davies, P. A. 1972 Experiments on Taylor columns in rotating stratified fluids. *J. Fluid Mech.* **54**, 691–717.

Davis, R. E. 1969 The two-dimensional flow of a stratified fluid over an obstacle. *J. Fluid Mech.* **36**, 127–143.

Fultz, D. & Spence, T. 1967 Preliminary experiments on baroclinic westerly flow over a north–south ridge. *Fort Collins, Col., Colorado State Univ., Atm. Sci. Pap.* no. 122, pp. 157–191.

Hide, R. 1966 On the dynamics of rotating fluids and related topics in geophysical fluid dynamics. *Bull. Am. Met. Soc.* **47**, 873–885.

Holton, J. R. 1979 *An introduction to dynamic meteorology* (Int. Geophys. Series vol. 23). Academic Press.

Honji, H., Taneda, S. & Tatsuno, A. 1980 Some practical details of the electrolytic precipitation method of flow visualization. *Res. Inst. Appl. Mech., Kyushu Univ.* **28**, 83–89.

Huppert, H. E. & Stern, M. E. 1974 The effect of side walls on homogeneous rotating flow over two-dimensional obstacles. *J. Fluid Mech.* **62**, 417–436.

Jacobs, S. J. 1964 On stratified flow over bottom topography. *J. mar. Res.* **22**, 223–235.

Kmetz, M. L. 1982 Vortex shedding in rotating flows. M.S. thesis, University of Wyoming, Laramie. (74 pages.)

Leach, H. 1981 Thermal convection in a rotating fluid: effects due to bottom topography. *J. Fluid Mech.* **109**, 75–87.

Long, R. R. 1955 Some aspects of the flow of stratified fluids. III. Continuous density gradients. *Tellus* **7**, 341–357.

Marwitz, J. D. 1983 The kinematics of orographic airflow during Sierra storms. *J. atmos. Sci.* **40**, 1219–1227.

Mason, P. J. 1975 Forces on spheres moving horizontally in a rotating stratified fluid. *Geophys. astrophys. Fluid Dyn.* **2**, 137–154.

Mason, P. J. & Sykes, R. I. 1978 On the interaction of topography and Ekman boundary layer pumping in a stratified atmosphere. *Q. Jl R. met. Soc.* **104**, 475–490.

Merkine, Lee-Or 1975 Steady finite-amplitude baroclinic flow over long topography in a rotating stratified atmosphere. *J. atmos. Sci.* **32**, 1881–1893.

Oster, G. 1965 Density gradients. *Scient. Am.* **213** (2), 70–76.

Parish, T. R. 1982 Barrier winds along the Sierra Nevada Mountains. *J. appl. Met.* **21**, 925–930.

Pedlosky, J. 1979 *Geophysical fluid dynamics*. Berlin: Springer-Verlag.

Pierrehumbert, R. T. 1984 Linear results on the barrier effects of mesoscale mountains. *J. atmos. Sci.* **41**, 1356–1367.

Pierrehumbert, R. T. 1985 Stratified semi-geostrophic flow over two-dimensional topography in an unbounded atmosphere. *J. atmos. Sci.* (In the press.)

Pierrehumbert, R. T. & Wyman, B. 1985 Upstream effects of mesoscale mountains. *J. atmos. Sci.* (In the press.)

Queney, P. 1947 Theory of perturbations in stratified currents with applications to air flow over mountain barriers. *Misc. Rep.* no. 23. (81 pages.) University of Chicago Press.

Robinson, A. R. 1960 On two-dimensional inertial flow in a rotating stratified fluid. *J. Fluid Mech.* **9**, 321–332.

Schwerdtfeger, W. 1974 Mountain barrier effect on the flow of stable air north of the Brooks Range. In *Proc. 24th Alaskan Science Conference, Geophysical Institute, University of Alaska, Fairbanks*, pp. 204–208.

Schwerdtfeger, W. 1975 The effect of the Antarctic Peninsula on the temperature regime of the Weddell Sea. *Mon. Weath. Rev.* **103**, 45–51.

Smith, R. B. 1979 The influence of mountains on the atmosphere. *Adv. Geophys.* **21**, 87–230.

Taneda, S., Honji, H. & Tatsuno, M. 1975 The behaviour of tracer particles in flow visualization by electrolysis of water. *J. phys. Soc. Japan* **37**, 784–788.

Taneda, S., Honji, H. & Tatsuno, M. 1977 The electrolytic precipitation method of flow visualization. In *Int. Symp. on Flow Visualization, Tokyo*, pp. 133–138.

Waight, K. T. III 1984 A numerical study of the Sierra Nevada barrier jet. *Dept. of Atm. Sci., Univ. of Wyoming Report* no. AS 148. (119 pages.)

Yeh, T. C. & Chang, C. C. 1974 A preliminary experimental simulation of the heating effect of the Tibetan plateau on the general circulation over eastern Asia in summer. *Scientia Sinica* **17**, 397–420.

PHILOSOPHICAL TRANSACTIONS OF THE ROYAL SOCIETY A MATHEMATICAL, PHYSICAL & ENGINEERING SCIENCES

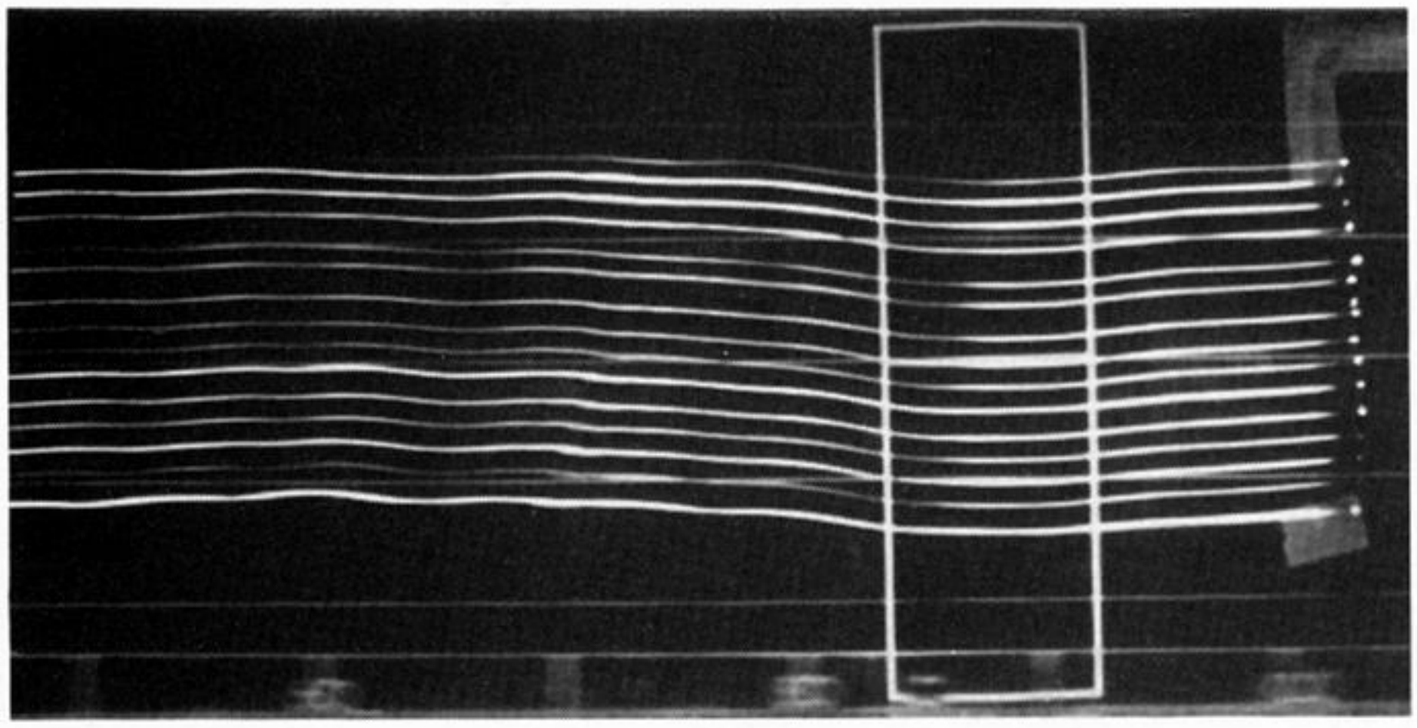

FIGURE 5. Vertical structure for fixed rotation, stratification (weak) and free stream speed: $Ro = 0.15$, $E = 1.5 \times 10^{-4}$ ($Re = 1540$), $B = 0.82$ ($\Delta\rho/\rho_0 = 5.6 \times 10^{-3}$), $h/H = 0.13$, $h/D = 0.11$ and $D/L = 0.32$.

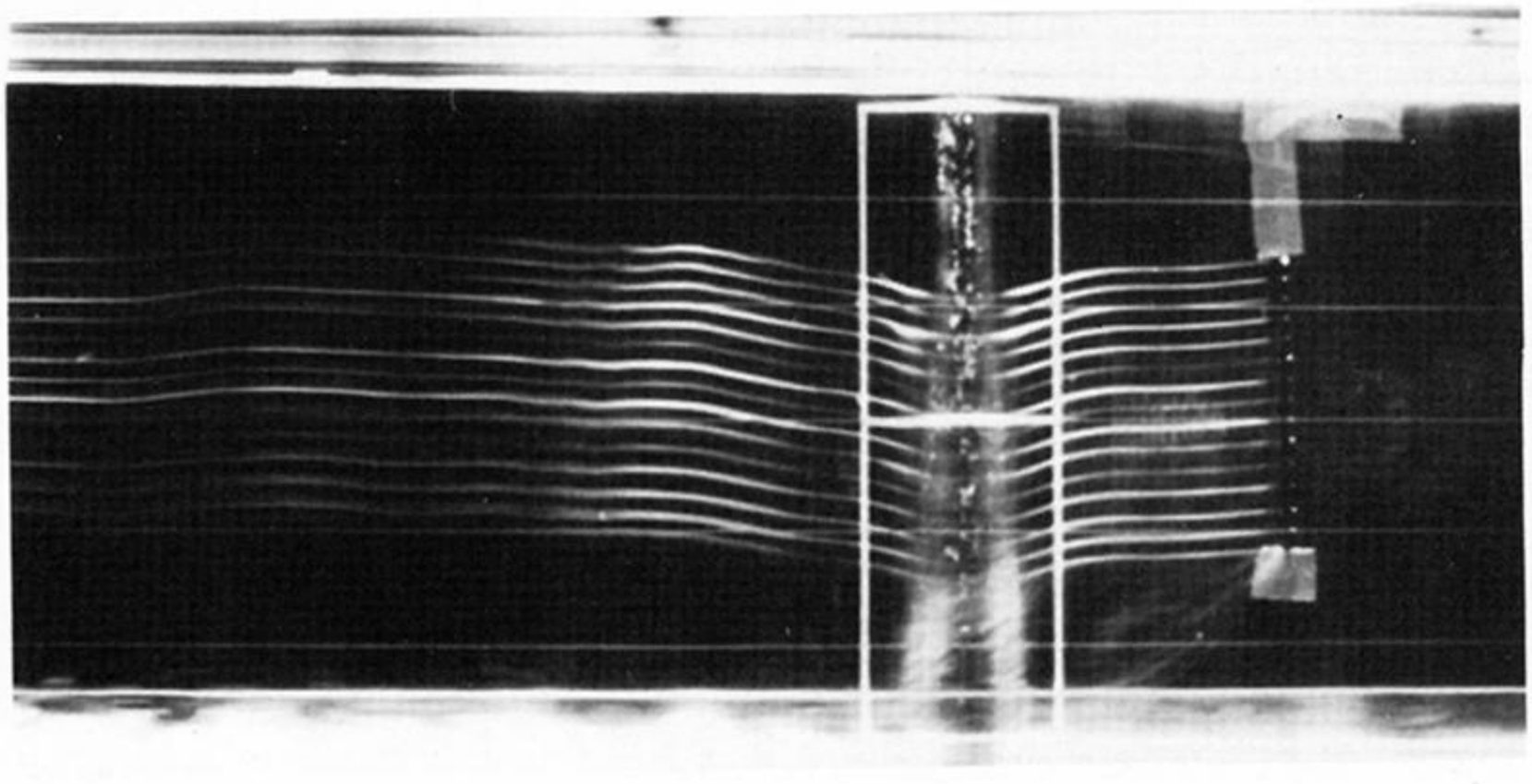

(a)

Ro	*Re*
0.15	1510

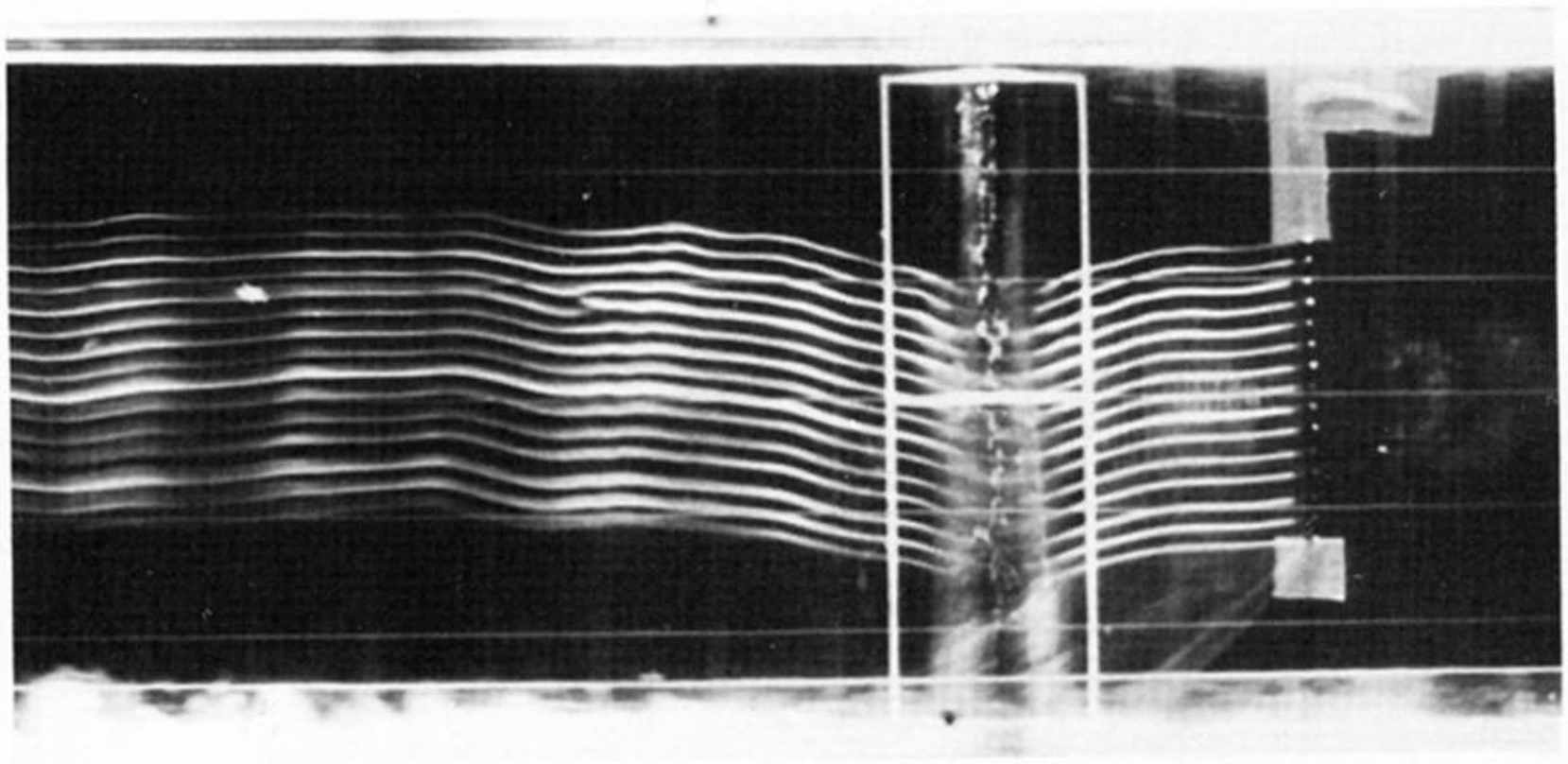

(b)

0.10	1010

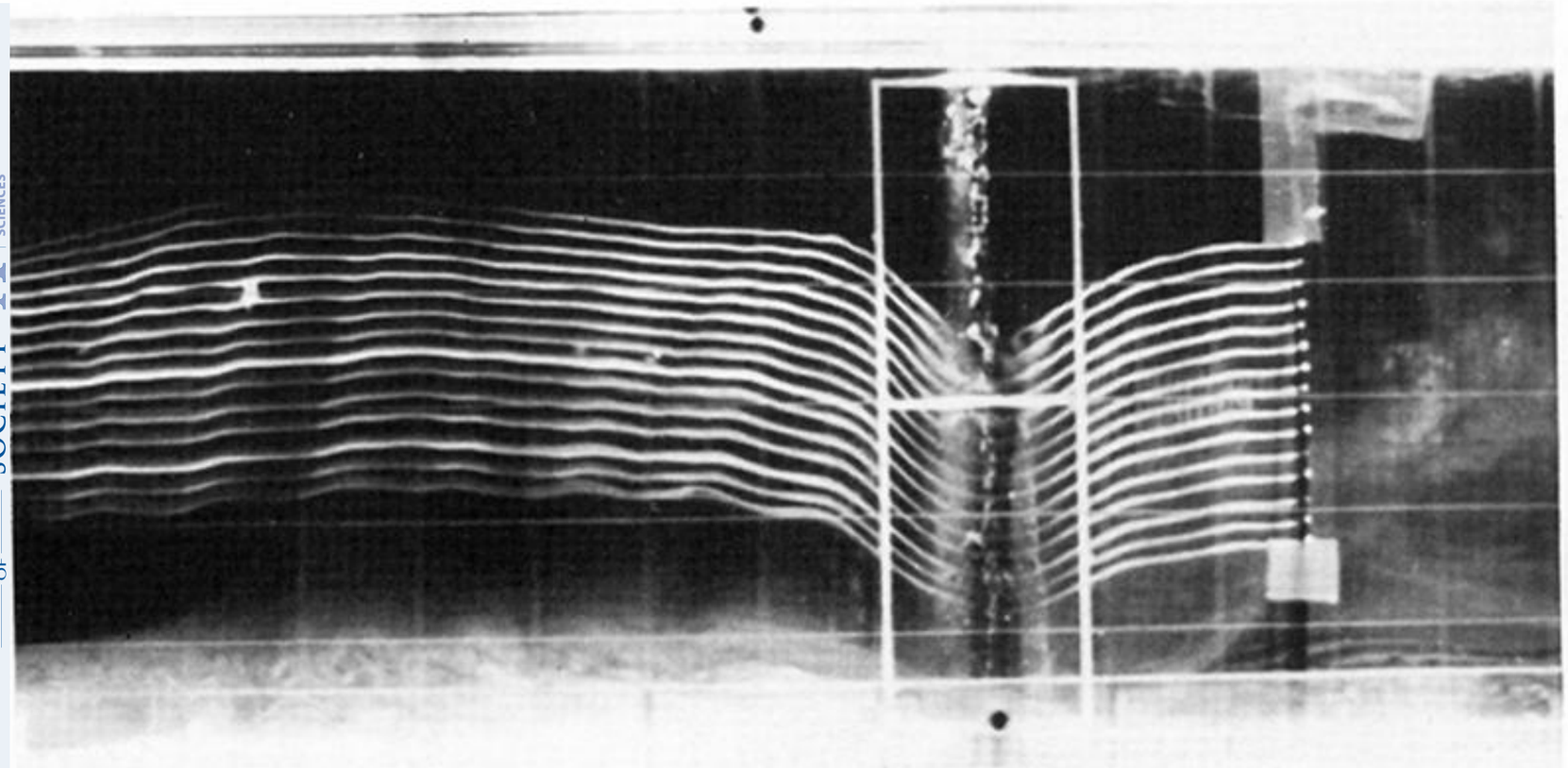

(c)

0.05	500

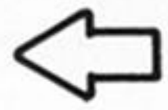

FIGURE 6. Free stream speed effects for fixed rotation and stratification (weak) as observed at ridge crest level: $z^*/h = 1.0$, $E = 1.5 \times 10^{-4}$, $B = 0.81$ $(\Delta\rho/\rho_0 = 5.4 \times 10^{-3})$, $h/H = 0.13$, $h/D = 0.11$ and $D/L = 0.32$. The horizontal line along the ridge centre is a marker on the ridge indicating the centreline of the channel.

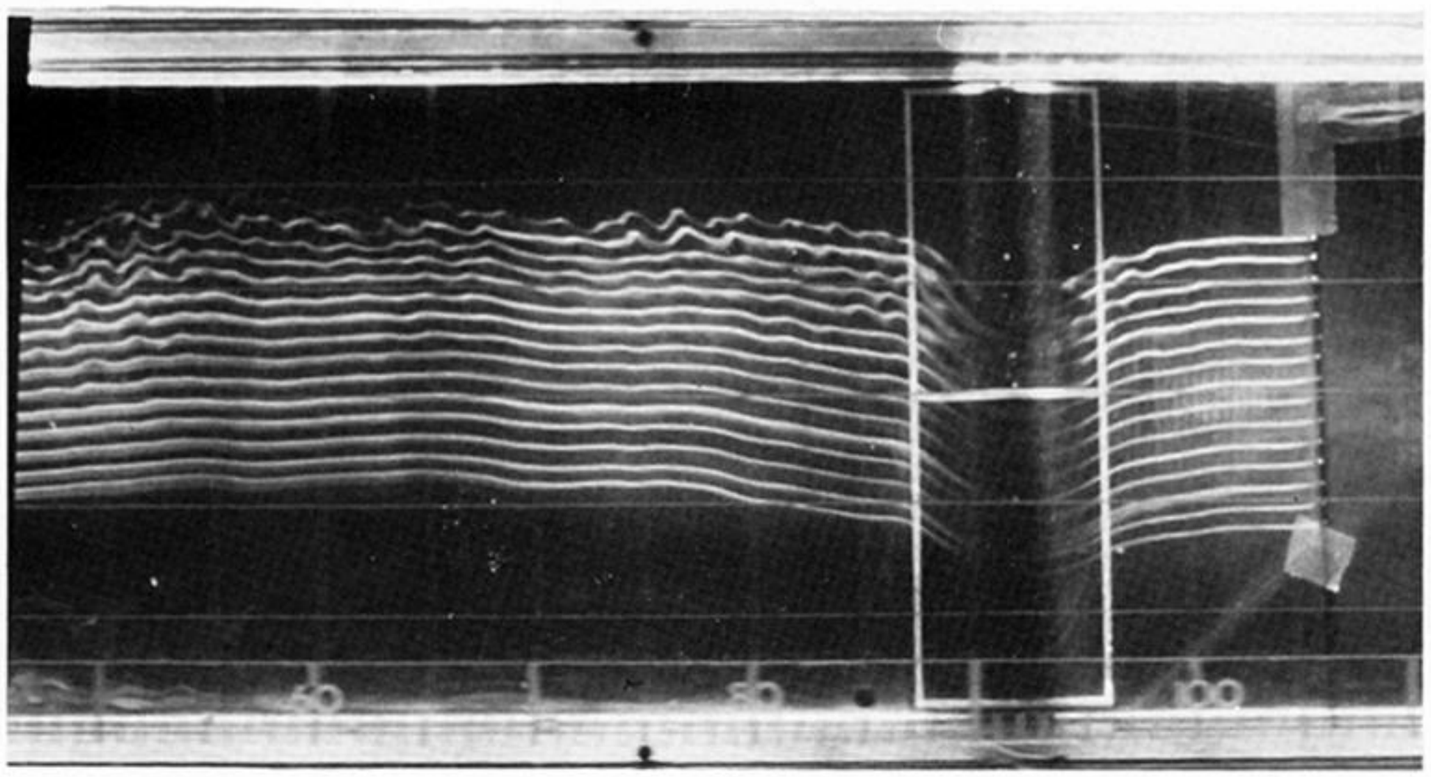

(*a*)

$\Delta\rho/\rho_0$	B
3.6×10^{-3}	1.33

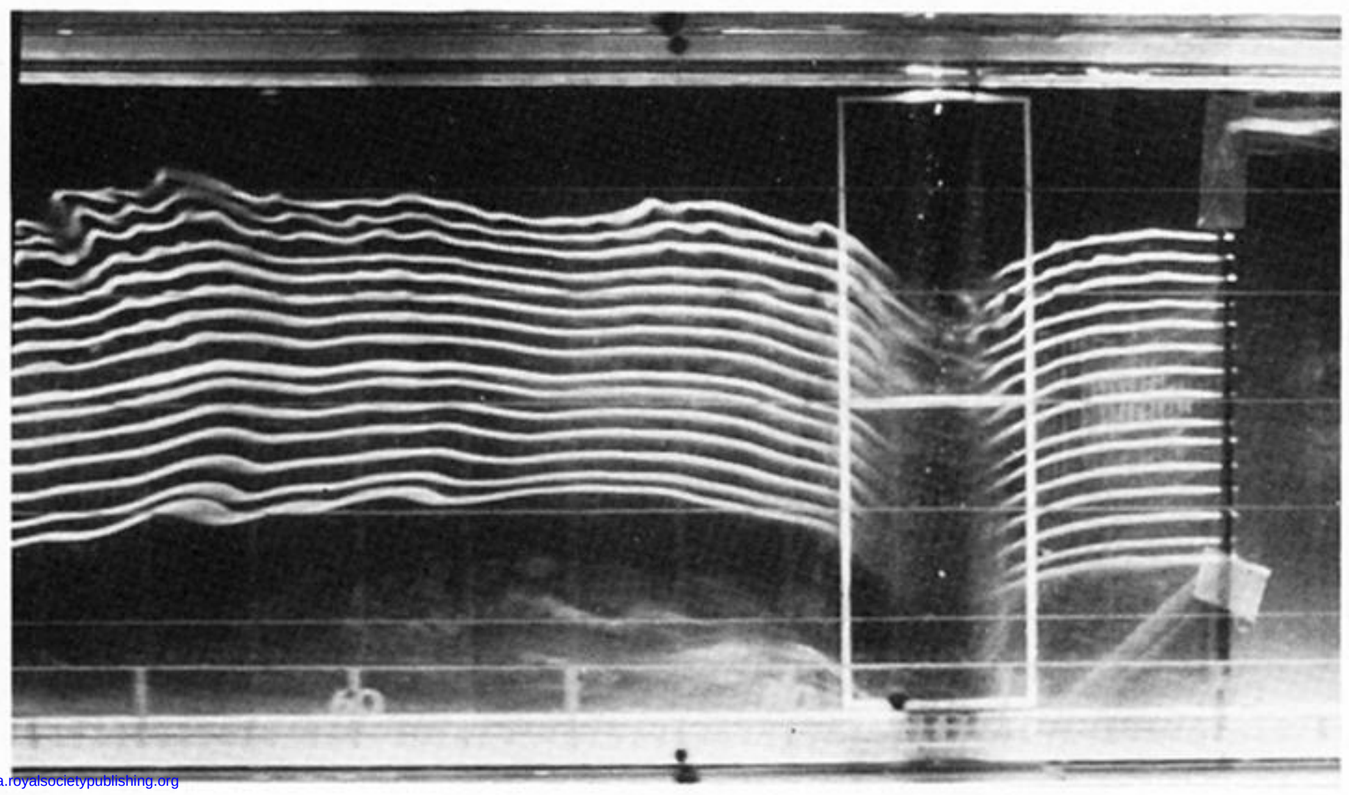

(*b*)

$\Delta\rho/\rho_0$	B
6.1×10^{-3}	1.71

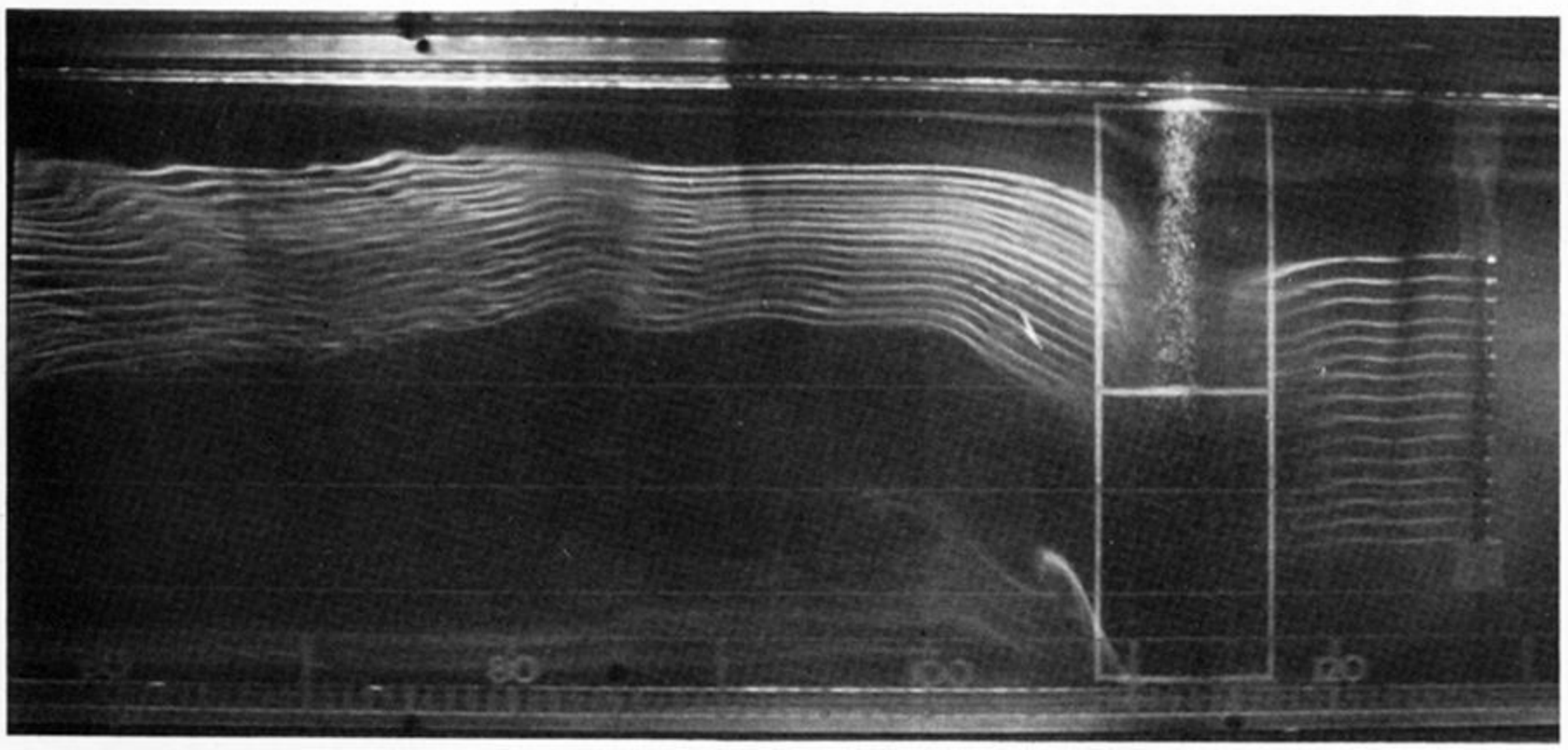

(*c*)

$\Delta\rho/\rho_0$	B
4.2×10^{-2}	4.49

FIGURE 7. Stratification effects for fixed rotation and free stream speed as observed at ridge crest level: $z^*/h = 1.0$, $Ro = 0.10$, $E = 3.0\times10^{-4}$ ($Re = 510$), $h/H = 0.13$, $h/D = 0.11$ and $D/L = 0.32$.

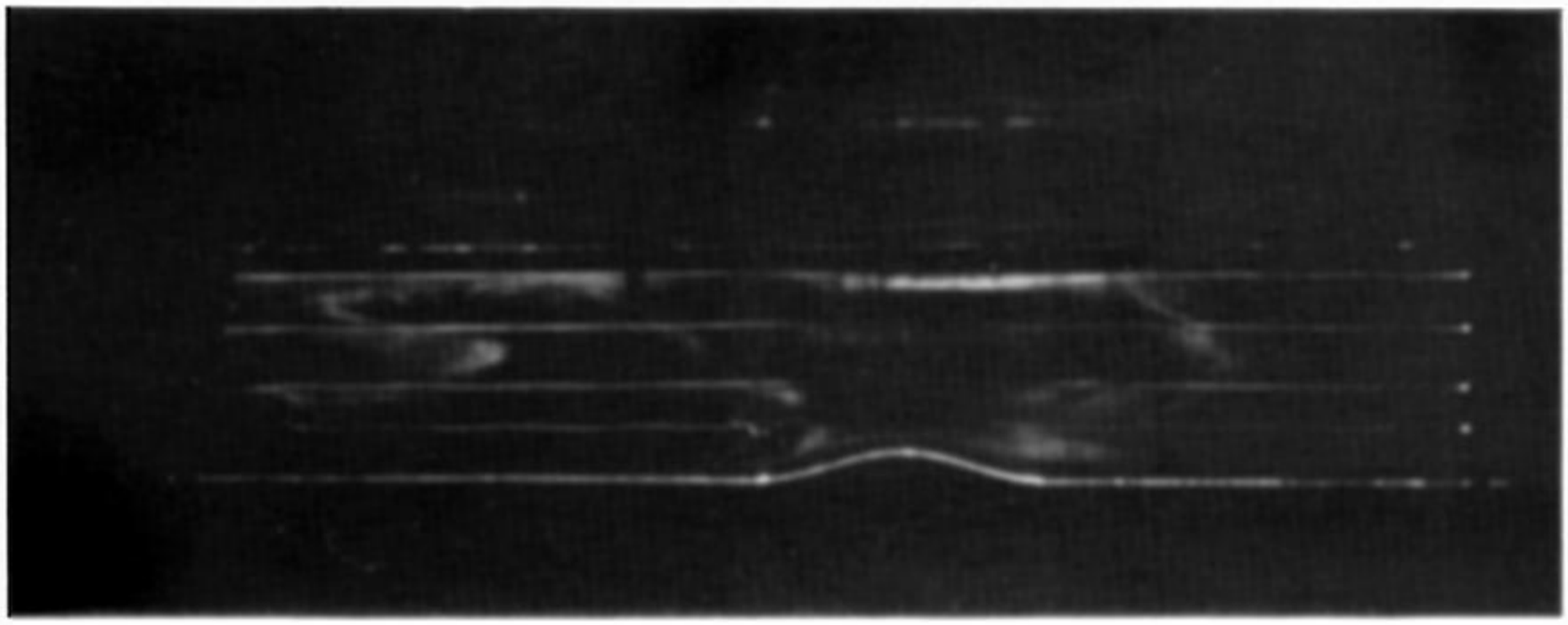

(*a*)

Ro	*Re*
0.10	520

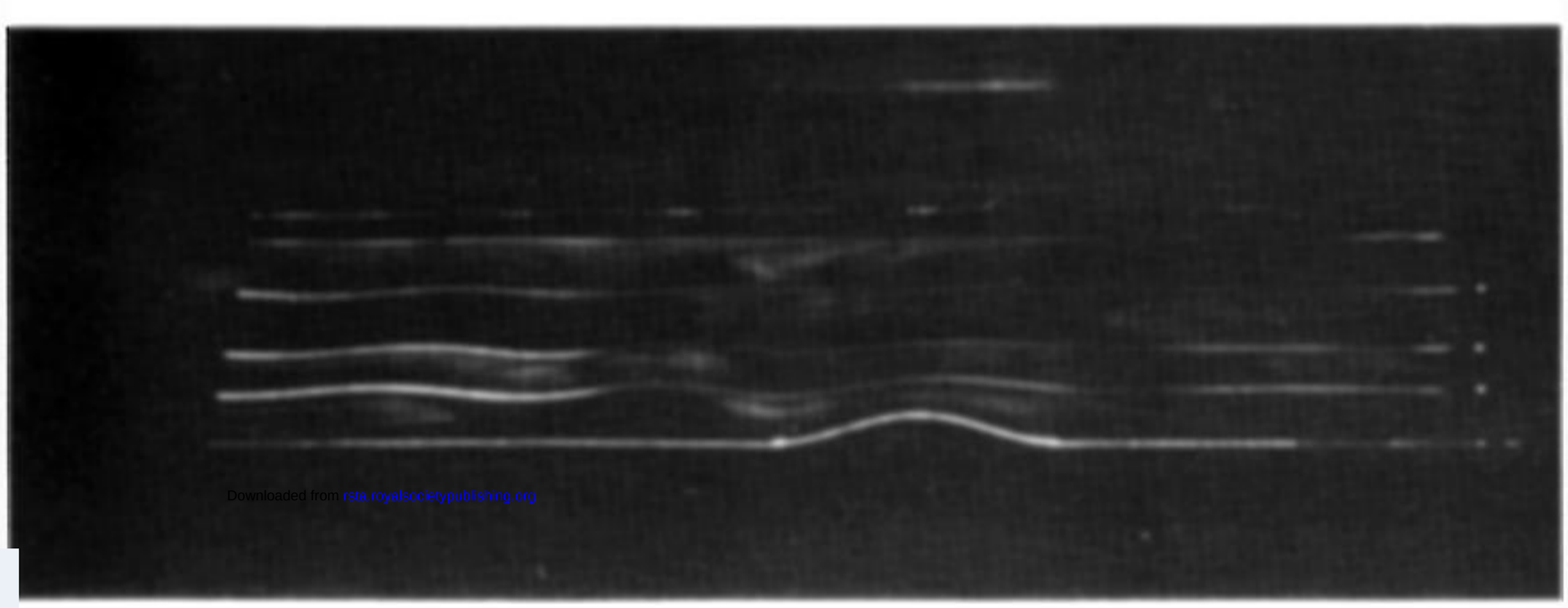

(*b*)

Ro	*Re*
0.20	1040

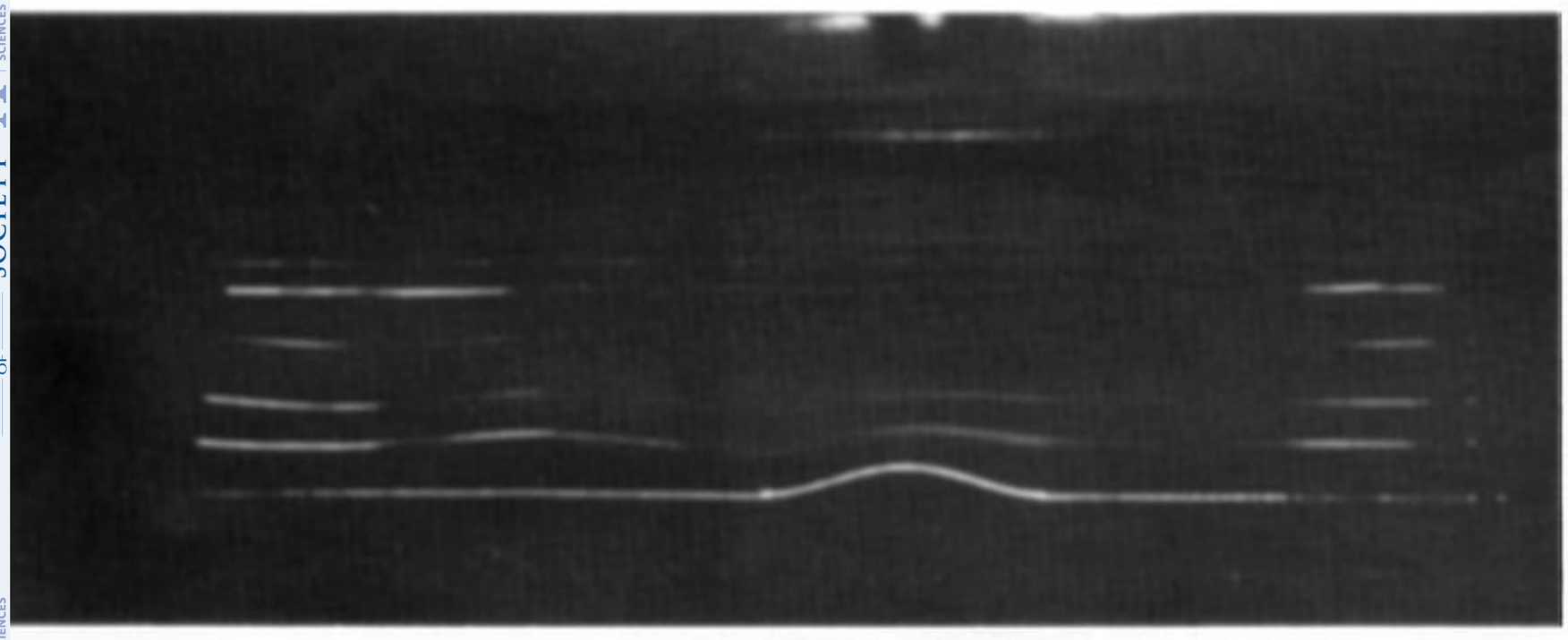

(*c*)

Ro	*Re*
0.30	1570

FIGURE 8. Free stream speed effects on lee wave structure for fixed rotation and stratification (weak): $E = 3.0 \times 10^{-4}$, $B = 1.33$ ($\Delta\rho/\rho_0 = 3.7 \times 10^{-3}$), $h/H = 0.13$, $h/D = 0.11$, $D/L = 0.32$ and $z^*/h = 1.7$, 3.2, 5.3 and 7.2. The white clouds in (*a*) and (*b*) are due to residual dye tracer from previous experiments and from dye tracer particles slightly heavier than the fluid medium 'dropping out' of the main streakline.

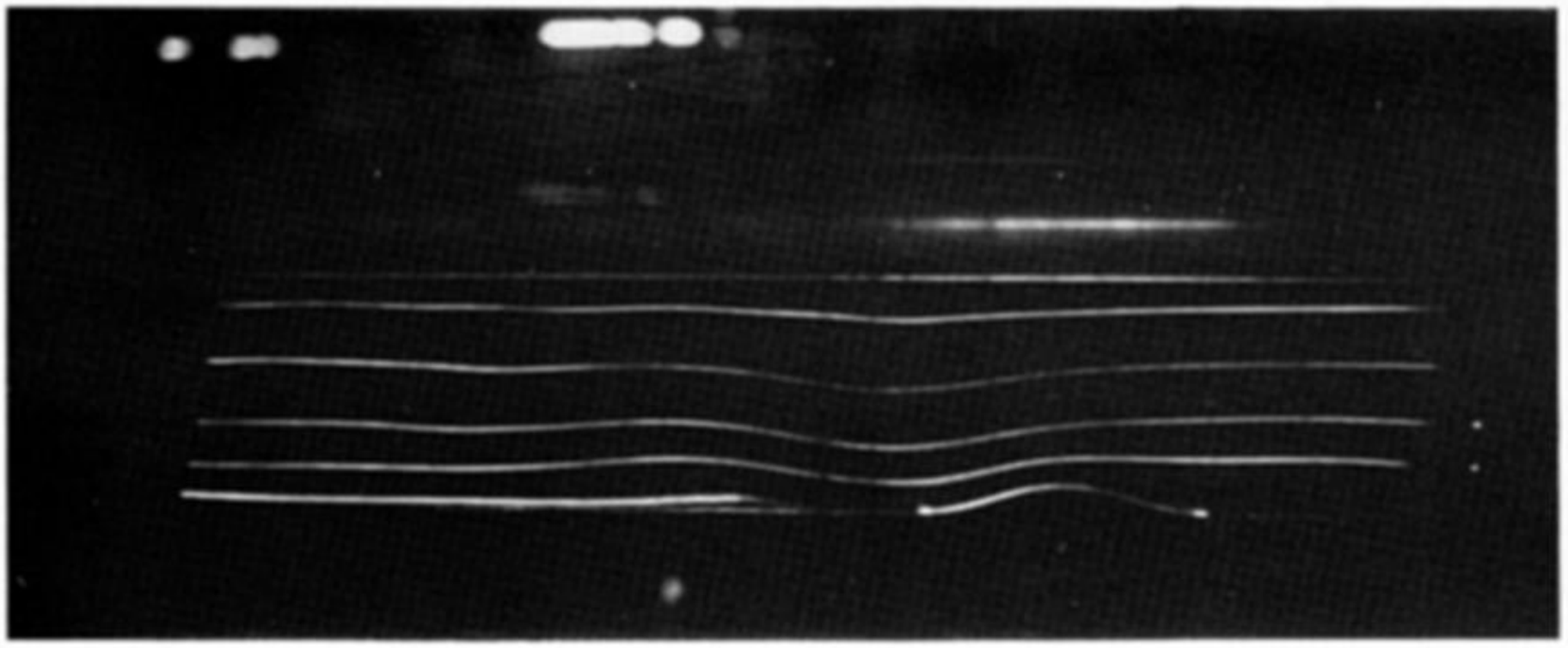

(*a*)

$\Delta\rho/\rho_0$

4.6×10^{-3}

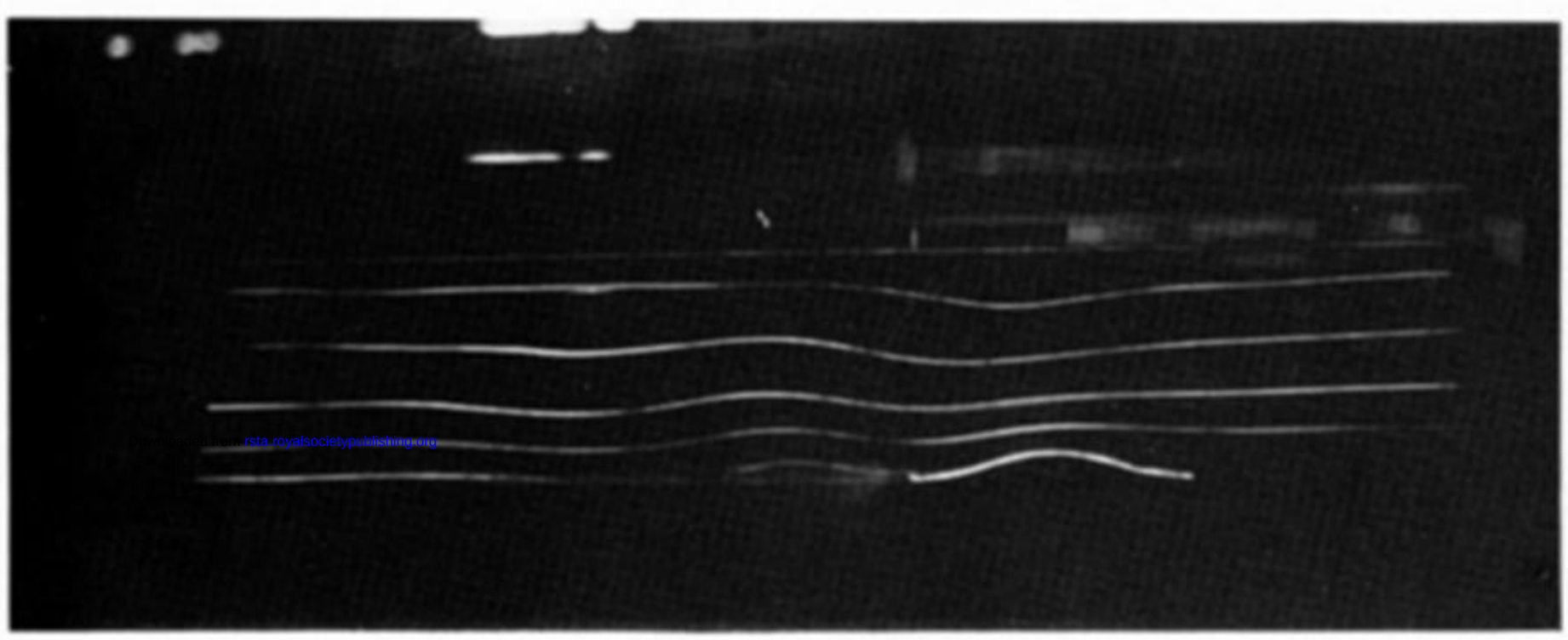

(*b*)

7.4×10^{-3}

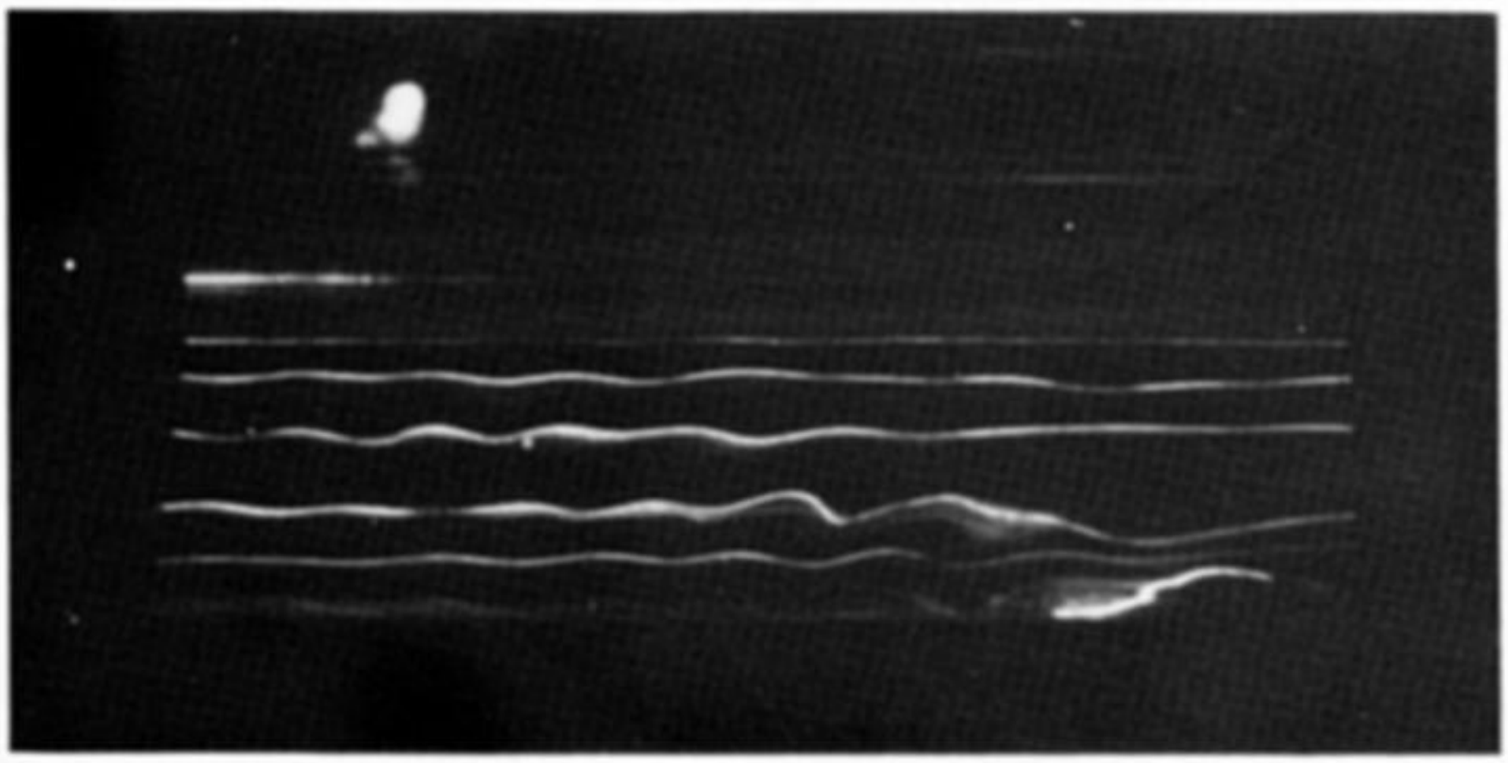

(*c*)

4.7×10^{-2}

U

FIGURE 9. Stratification effects on lee wave structure for zero rotation and fixed free stream speed: $Re = 510$, $h/H = 0.13$, $h/D = 0.11$ and $z^*/h = 1.7$, 3.2, 5.3 and 7.2.

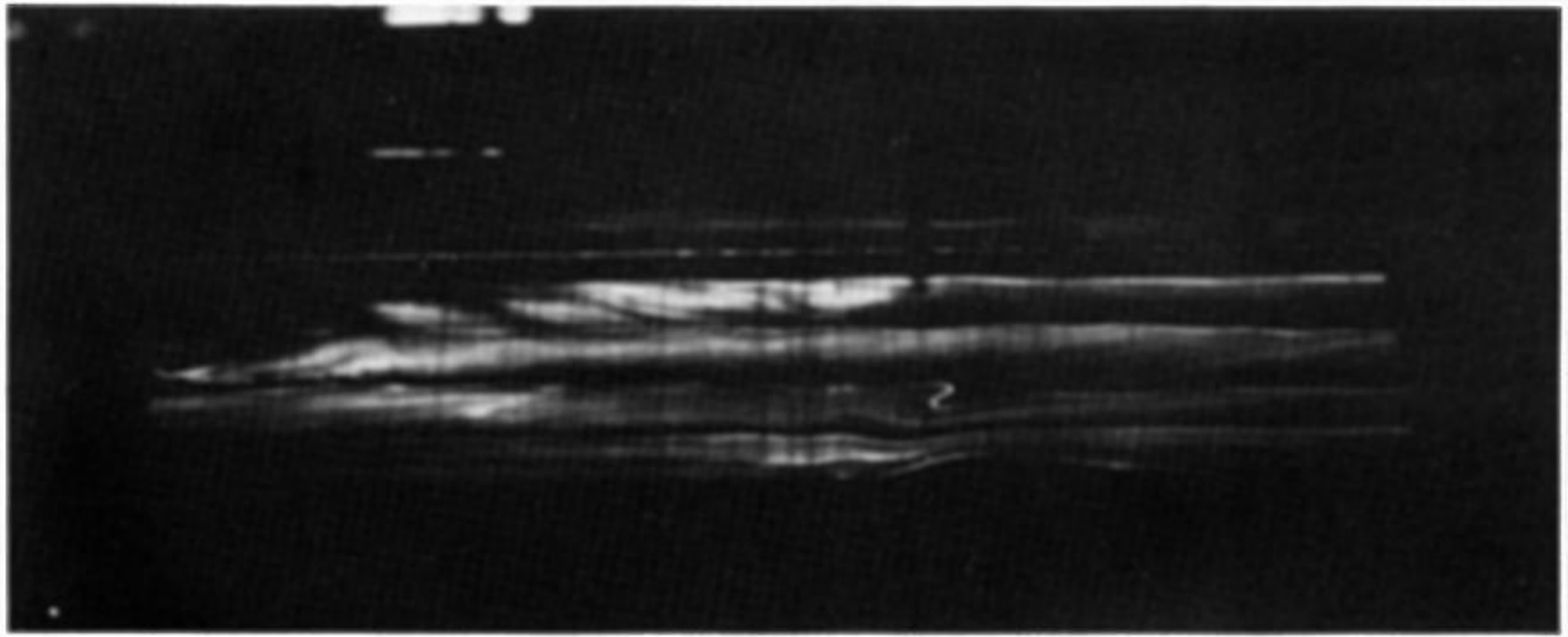

GURE 11. S-shaped streakline for unsteady non-rotating flow: $Re = 500$, $F_i = 0.069$ $(\Delta\rho/\rho_0 = 6.5 \times 10^{-3})$, $h/H = 0.13$, $h/D = 0.11$ and $z^*/h = 1.7$, 3.2, 5.3 and 7.2. See caption of figure 8 concerning white clouds in photograph.

PHILOSOPHICAL TRANSACTIONS OF THE ROYAL SOCIETY A MATHEMATICAL, PHYSICAL & ENGINEERING SCIENCES

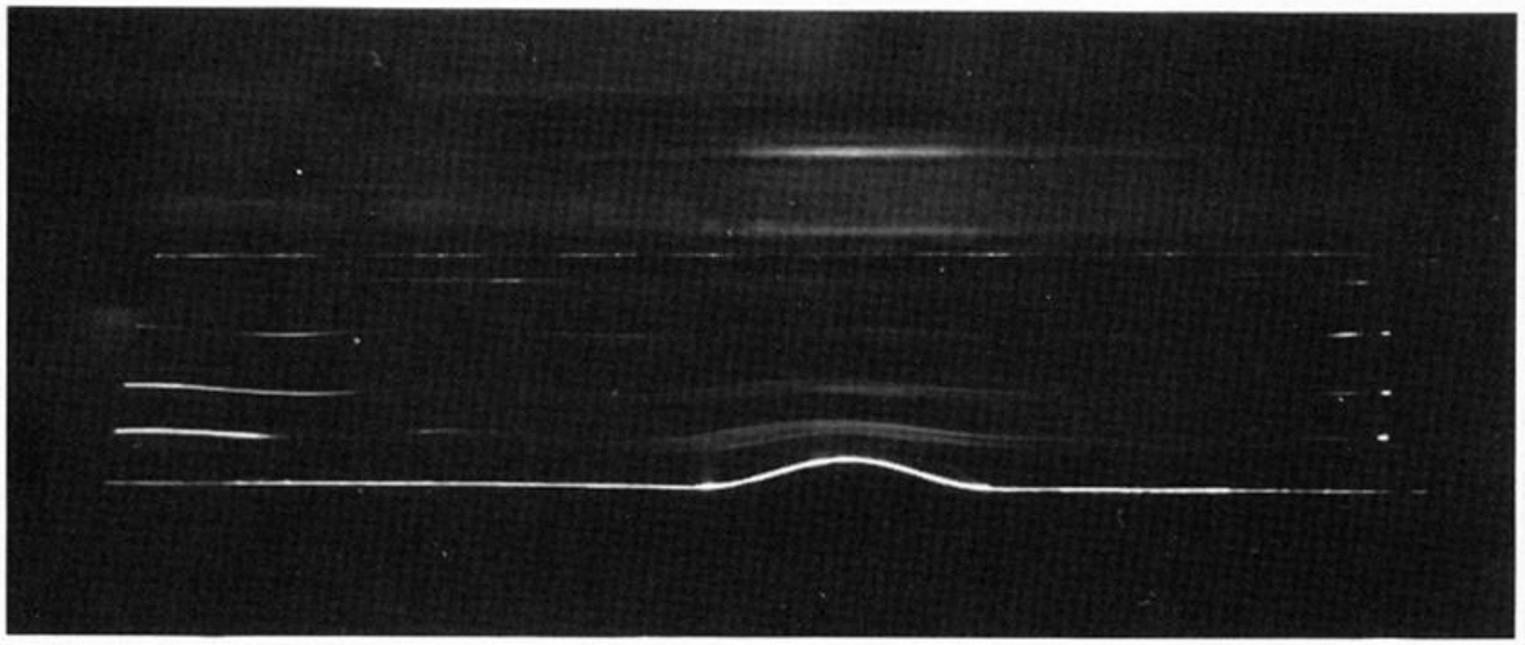

(a)

$\Delta\rho/\rho_0$	B
3.9×10^{-3}	0.68

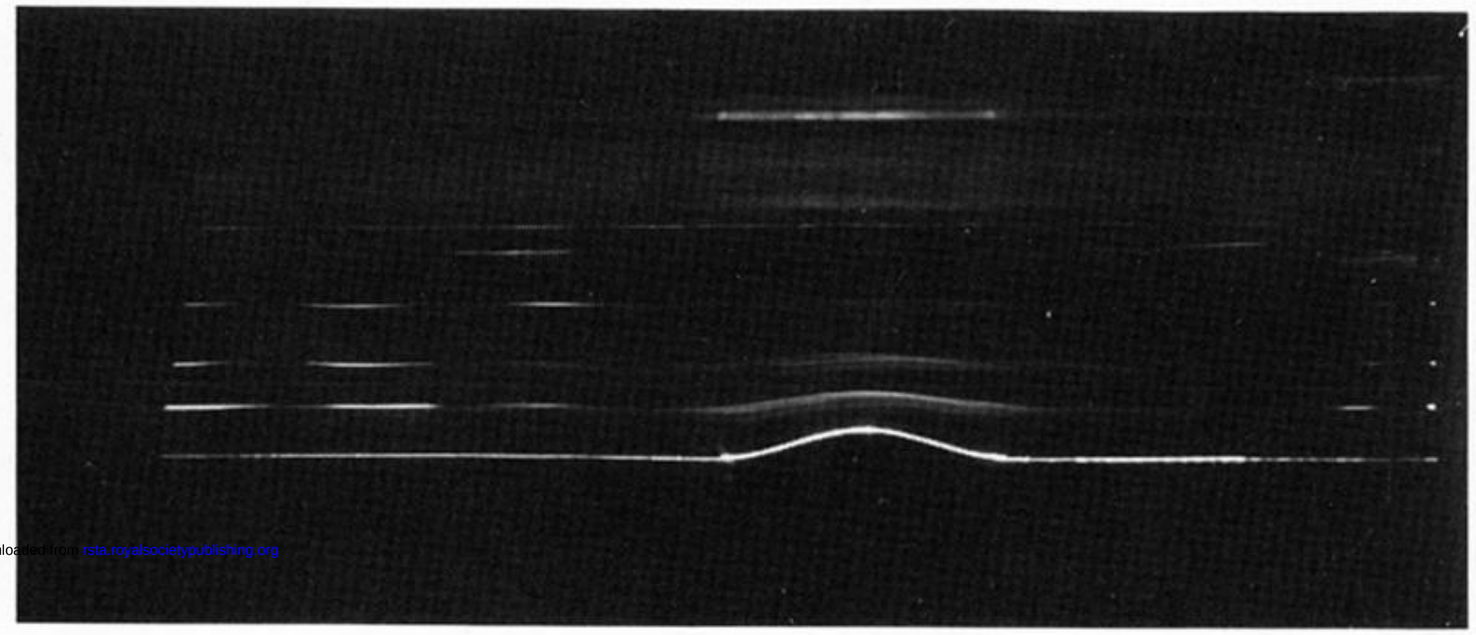

(b)

$\Delta\rho/\rho_0$	B
6.1×10^{-3}	0.86

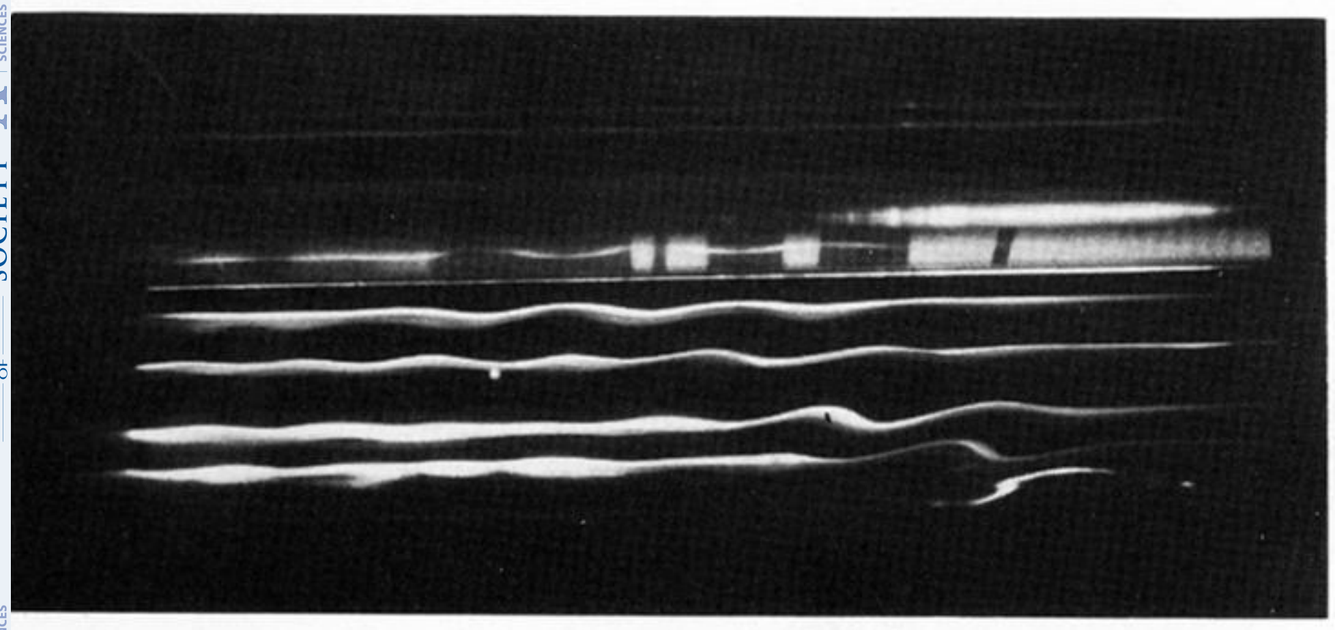

(c)

$\Delta\rho/\rho_0$	B
4.3×10^{-2}	2.28

FIGURE 12. Stratification effects on lee wave structure for fixed rotation and free stream speed: $Ro = 0.15$, $E = 1.5\times10^{-4}$ ($Re = 1510$), $h/H = 0.13$, $h/D = 0.11$, $D/L = 0.32$ and $z^*/h = 1.7$, 3.2, 5.3 and 7.2.

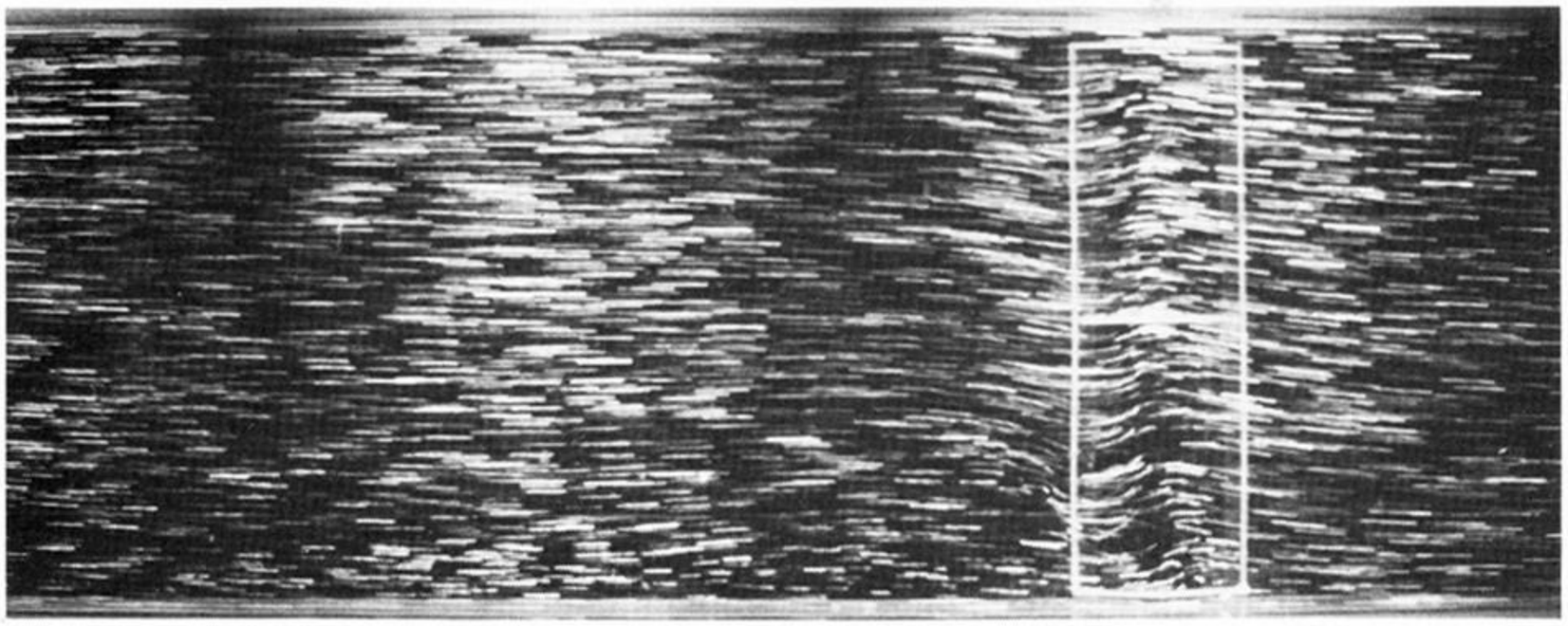

FIGURE 13. Particle streak photographs of horizontal patterns at levels $z^*/h = 3.0$, 2.0 and 1.0 (i.e. (*a*), (*b*), (*c*) respectively) and vertical mode 5 pattern at $y^*/D = 0.0$ (i.e. (*d*)); $Ro = 0.25$, $E = 8.2 \times 10^{-4}$ ($Re = 470$), $B = 6.3$ ($\Delta\rho/\rho_0 = 1.1 \times 10^{-2}$), $h/H = 0.13$, $h/D = 0.11$, $D/L = 0.32$. Note that the horizontal scale in (*d*) is three times that in (*a*), (*b*) and (*c*).